JOURNAL OF GEOPHYSICAL RESEARCH, VOL. 99, NO. D9, PAGES 18,713–18,733, SEPTEMBER 20, 1994

Sulfur dioxide oxidation in winter orographic clouds

Jefferson R. Snider and Gabor Vali
Department of Atmospheric Science, University of Wyoming, Laramie

ABSTRACT. The production of sulfate in cloud droplets, and the attendant depletion of sulfur dioxide (SO_2) oxidants were studied in wintertime orographic clouds over southeastern Wyoming. By periodic (5-20 min) releases of SO_2 into the cloud the mixing ratio of SO_2 was raised to about double its background value of 0.7 parts per billion by volume (ppbv). Average values of the in-cloud reaction time, pseudo-first-order SO_2 reaction rate, and hydrogen peroxide (H_2O_2) depletion were 400 s, 2.3 x 10^{-4} s^{-1}, and 0.04 ppbv, respectively. The measured sulfate yields and H_2O_2 depletions show that H_2O_2 is the dominant oxidant for SO_2 in this situation; this finding is consistent with model results. Model simulations reveal that the O_2/SO_2 reaction pathway (catalyzed by Mn(II) and Fe(III)) was competitive with the H_2O_2/SO_2 reaction pathway on one out of the nine observation days. Organohydroperoxides were not depleted and other modeled reaction pathways (O_3/SO_2 and $HCHO/SO_2$) were inferred to be inhibited due to either the chemical (pH < 4.7) or physical (temperature below -5 °C, cloud water content less than 0.3 cm^3 m^{-3}) properties of the cloud. The agreement found in this work between observed and predicted properties of the $H_2O_2/SO_2/H_2O$ system contrasts with the work of Chandler et al. (1988a, b, 1989) and Gallagher et al. (1990) who observe a factor of 3 or larger discrepancy between laboratory and field measurements of the H_2O_2/SO_2 reaction rate.

1. Introduction

The dominant sources of atmospheric sulfur dioxide (SO_2) are man-made emissions and the gas phase oxidation of biogenic dimethylsulfide [*Warneck*, 1988]. Reaction of SO_2 occurs via a variety of pathways. Gas phase reaction with the hydroxyl radical leads to a SO_2 half-life of 7-14 days under conditions typical of midlatitude wintertime insolation [*Calvert et al.*, 1985]. In comparison, the reactions of SO_2 dissolved in cloud droplets yield lifetimes 10-100 times shorter. Therefore in-cloud reactions constitute a major factor for regional and for global removal of SO_2. The quoted range of in-cloud lifetimes is based on laboratory kinetic investigations of the hydrogen peroxide (H_2O_2) and ozone (O_3) reactions with sulfur in the +4 oxidation state (S(IV)) [*Hoffmann and Calvert*, 1985; *Hoffmann*, 1986] and on data obtained in field studies [*Hegg and Hobbs*, 1982; *Gervat et al.*, 1988]. However, there are important uncertainties in these values.

Model calculations based on field observations conducted in northern England [*Chandler et al.*, 1988a, b, 1989; *Gallagher et al.*, 1990] suggest that the H_2O_2-S(IV) reaction rate constants determined either using purified water (*Hoffmann and Calvert*, 1985] or using authentic precipitation samples [*Lee et al.*, 1986] are a factor of 3-10 too low. The field studies themselves involve important uncertainties, mostly in regard to measurements of the depletion of H_2O_2. A small number of simultaneous measurements of sulfate production and of H_2O_2 depletion were obtained in experiments conducted at Great Dun Fell in the United Kingdom [*Chandler et al.*, 1989; *Clark et al.*, 1990; *Gallagher et al.*, 1990]. Such data are essential if the field experiments are to be compared reliably with laboratory data and if they are to lead to identification of the dominant reaction pathways for SO_2. This information is necessary for reliable assessments of how changes in SO_2 emissions will affect sulfuric acid deposition.

To help clarify the questions just discussed, studies of SO_2 oxidation to sulfate have been conducted at a remote continental site in southeastern Wyoming (United States) with controlled releases of SO_2 into nonprecipitating orographic clouds. A pseudo-first-order reaction rate for SO_2 oxidation in cloud water, reactant depletions, and sulfate yields are deduced from the observations. Model predictions of the amount of sulfate produced by the various reaction pathways are also examined. The models afford an examination of the present understanding of SO_2 reactivity in cold clouds of low liquid water content, similar to those in which the observations were made.

Copyright 1994 by the American Geophysical Union.

Paper number 94JD01522.
0148-0227/94/94JD-01522$05.00

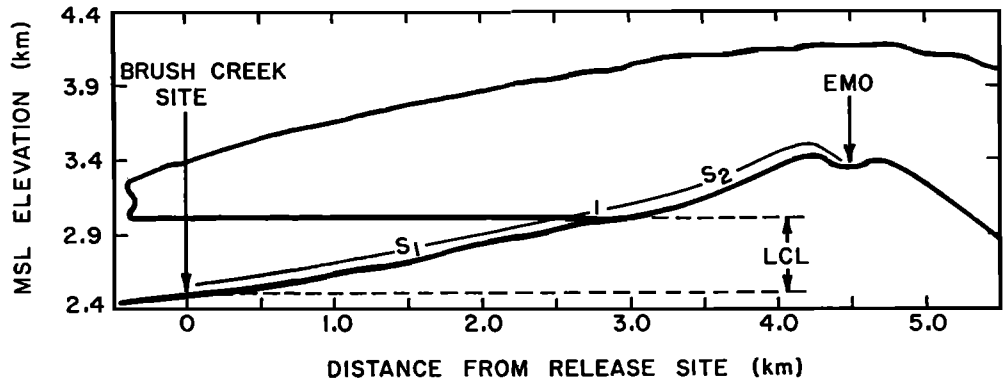

Figure 1. Cross section of Elk Mountain along the Brush Creek drainage. The Brush Creek site is located southwest of Elk Mountain Observatory (EMO). Gaseous SO_2 and SF_6 were released at the Brush Creek site and detected at EMO. The lifted condensation level (LCL) and gas transport distances below cloud (S_1) and in cloud (S_2) are illustrated.

2. Experimental Site: Elk Mountain Observatory

The Elk Mountain Observatory (EMO) (see Figure 1), is located at 3.3 km altitude (above mean sea level (msl)) in a col near the western summit of Elk Mountain (3.4 km msl). During these experiments all gas phase chemistry measurements and cloud water sampling were conducted at EMO.

Instrumentation at the EMO facility consisted of a wind sensor located on the western summit, meteorological sensors mounted on a platform 5 m above the snow surface and 10 m west of the observatory building, rime ice collectors also located on the platform, and a Commonwealth Scientific and Industrial Research Organization (CSIRO) probe [*King et al.*, 1978] mounted in a wind tunnel next to the platform. Air intake for the gas phase chemistry instrumentation, located within the observatory building, was through an inverted J pipe of 7.3 cm diameter.

The Brush Creek site, where a PAM-II automated weather station [*Brock et al.*, 1986] and the gas release system were located, is 4.5 km southwest of EMO at an elevation of 2.5 km msl. The release of either SF_6 or SO_2 could be initiated from EMO via radio signals. The field experiments were conducted during periods when the EMO was enveloped in "cap" clouds and when southwesterly surface winds provided effective channeling of the flow to the EMO along Brush Creek canyon. SF_6 releases (duration 1-5 min) were conducted before, during, and after longer-duration (≈15 min) SO_2 releases. In some of the field experiments, cloud base elevation was determined using pilot balloons released from the Brush Creek site.

3. Methods

3.1. Composition of Air and Cloud Water

Instruments for continuous measurement of SF_6 (Scientech Incorporated, model LBF-3), SO_2 (Columbia Scientific Industries, model SA-260), hydroperoxides [*Lazrus et al.*, 1986], and O_3 (Thermoelectron Corporation, model 49) were operated at EMO. Analog signals from these devices were recorded at 1 Hz using a Hewlett Packard MX-1000 minicomputer. Further details on sensor response times and analytical precision are available elsewhere [*Snider et al.*, 1992].

Cloud water samples were collected at EMO as rime ice deposits, using a rotating dual-arm wire grid [*Snider et al.*, 1992]. Since concurrent measurements of cloud droplet number concentration or size were not conducted, only estimates of the droplet capture efficiencies, based on droplet spectra summarized in both *Rogers et al.* [1983] and in *Politovich and Vali* [1983], can be provided. The results of *Langmuir and Blodgett* [1946] and the interval-averaged collector width (1.5 mm) were used in the calculations. For the liquid water mass distribution reported by *Rogers et al.* [1983] (mass-median radius = 6.5 μm, standard deviation = 2.0 μm) the capture efficiency is 0.85 (The value previously reported (0.78) for the capture efficiency [*Snider et al.*, 1992] was incorrect due to an error in our interpretation of the Langmuir and Blodgett equations). The capture efficiency decreases to 0.73 if the distribution is described by smaller values of mass-median radius (4 μm) and standard deviation (1 μm). The latter values of capture efficiency and droplet radius are thought to be representative of conditions during experiments associated with values of the cloud liquid water content (LWC) ($cm^3\ m^{-3}$) smaller than 0.1 $cm^3\ m^{-3}$. The droplet radius corresponding to a capture efficiency of 50% is 2 μm; this value is independent of the drop size distribution.

Melted rime ice samples were analyzed for hydroperoxides using the technique of *Kok et al.* [1986]. Delays between sample collection and the addition of the hydroperoxide reagent were 0.5-4 hours. Approximately 1 in 10 samples were also tested for dissolved organohydroperoxides by adding catalase enzyme prior to addition of the hydroperoxide reagent. Organohydroperoxide concentrations were always less than 10% of the concentration of H_2O_2 ($[H_2O_2]$, M) and therefore differences between the sum of all hydroperoxide concentrations and $[H_2O_2]$ were ignored.

For the experiments conducted in 1987 and 1988, *p*H values and the concentrations of inorganic anions (Cl^-, NO_3^-, SO_4^{2-}), inorganic cations (NH_4^+, Na^+, K^+, Mg^{2+}, Ca^{2+}), and the acetic and formic acid species (CH_3CO_2H, HCO_2H) were measured 2-10 days after sample collection. Samples were preserved by refrigeration. The sample aliquots used for the organic acid and the inorganic cation analyses were

treated with chloroform to inhibit microbial degradation. Analytical techniques consisted of ion chromatography for inorganic anions (Dionex HPIC-AS4 and AMMS-1 columns, 4 mM $NaHCO_3$/1 mM Na_2CO_3 eluent), monovalent cations (Dionex HPIC-CS1 and CMMS-1 columns, 5 mM HCl eluent), and for the organic acid anions (Dionex APIC-AS4 and AMMS-1 columns, 22 mM $Na_2B_4O_7$ eluent). Divalent cations were analyzed using flame atomic absorption spectroscopy. Sample *p*H was determined using a glass electrode (Orion model 811500). Concentrations of the formic acid species were 2-3 times larger than those of the acetic acid species. Because of this concentration difference and because of the smaller pK_A of HCO_2H, only the formic acid data were considered in the model studies. During the 1989 experiments, inorganic anion concentrations and *p*H were determined within 30 min of sample collection.

3.2. Derived Quantities

Hydrogen peroxide depletion ($D_{H_2O_2}$, parts per billion by volulme (ppbv)) is derived from averages of total H_2O_2 (gas plus aqueous) during SO_2 plume ($X^p_{H_2O_2}$) and background ($X^b_{H_2O_2}$) sampling intervals:

$$D_{H_2O_2} = X^b_{H_2O_2} - X^p_{H_2O_2} \quad (1)$$

We calculate $X_{H_2O_2}$ as the sum of the gas phase H_2O_2 mixing ratio and the amount of H_2O_2 measured in the cloud water samples (also expressed as a gas phase mixing ratio). This assumption is substantiated by *Snider et al.* [1992]. Values of the organohydroperoxide depletion (D_{ORGA}, ppbv) are calculated in a manner similar to (1) but neglecting any contribution from cloud-water-dissolved organohydroperoxide. Errors in D_{ORGA} and $D_{H_2O_2}$ arise from uncertainties in the calibration (±10%) and zeroing (±0.005 ppbv) of the hydroperoxide monitor. Errors in $D_{H_2O_2}$ also arise from errors in the measurement of LWC performed at EMO (L_{EMO}, $cm^3\ m^{-3}$) and from errors in $[H_2O_2]$. Observed values of D_{ORGA} and $D_{H_2O_2}$, and the corresponding experimental uncertainties, are shown in Table 1. Relative biases in $D_{H_2O_2}$ as large as +30% may occur if the fraction of H_2O_2 in cloud droplets smaller than 2 μm is not accounted for. This is unlikely, however, since a significant fraction of the cloud-water-dissolved H_2O_2 is sampled by the hydroperoxide monitor [*Snider et al.*, 1992].

Yields of sulfate (Y_{SO_4}, ppbv) and nitrate (Y_{NO_3}, ppbv) are derived from the concentrations of sulfate ($[SO_4^{2-}]$, M) and nitrate ($[NO_3^-]$, M) and the appropriate EMO temperature (T_{EMO}, K) and pressure ($P_{EMO} = 0.67 \times 10^{+5}$ Pa):

$$Y_{SO_4} = \frac{10^9(L^p_{EMO}[SO_4^{2-}]^p - L^b_{EMO}[SO_4^{2-}]^b)C_1RT_{EMO}}{P_{EMO}} \quad (2)$$

$$Y_{NO_3} = \frac{10^9(L^p_{EMO}[NO_3^-]^p - L^b_{EMO}[NO_3^-]^b)C_1RT_{EMO}}{P_{EMO}} \quad (3)$$

Table 1. Yields, Depletions, and Experimental Uncertainties

ID	$D_{H_2O_2}$, ppbv	$\sigma_{DH_2O_2}$, ppbv	D_{ORGA}, ppbv	σ_{DORGA}, ppbv	Y_{SO_4}, ppbv	σ_{YSO_4}, ppbv	Y_{NO_3}, ppbv	σ_{YNO_3}, ppbv
52	na		na		0.002	0.005	0.014	0.004
53	na		na		0.014	0.005	0.003	0.007
84	0.033	0.007	0.003	0.005	-0.004	0.021	-0.007	0.031
89	0.033	0.014	-0.004	0.005	0.029	0.030	0.015	0.043
8B	0.029	0.013	-0.002	0.005	0.034	0.024	0.042	0.036
8X	0.036	0.014	0.001	0.005	0.017	0.040	-0.016	0.059
94	0.081	0.015	0.004	0.005	0.049	0.048	-0.035	0.060
B1	0.037	0.009	na		na		na	
2E	0.007	0.007	-0.003	0.005	0.023	0.010	-0.007	0.008
2G	0.003	0.007	0.000	0.005	0.005	0.010	-0.004	0.008
2J	0.001	0.008	-0.001	0.005	0.019	0.016	0.020	0.021
2L	0.010	0.008	0.000	0.005	0.012	0.016	0.014	0.021
2N	0.004	0.008	0.002	0.005	0.010	0.022	-0.001	0.042
43	0.004	0.007	0.002	0.005	0.012	0.004	0.003	0.006
66	0.247	0.030	0.002	0.005	0.224	0.048	0.010	0.031
8D	0.014	0.017	-0.003	0.005	0.014	0.023	-0.011	0.042
8F	0.019	0.019	0.002	0.005	0.074	0.029	0.072	0.061
8H	0.030	0.019	-0.002	0.005	0.033	0.029	-0.003	0.061
8J	0.055	0.010	0.000	0.005	0.031	0.014	0.067	0.028
CX	0.037	0.016	0.007	0.005	na		na	
C1	0.028	0.016	-0.004	0.005	0.034	0.017	-0.009	0.027
C4	0.037	0.014	-0.007	0.005	0.051	0.017	0.002	0.027
C6	0.027	0.020	-0.007	0.005	0.023	0.025	0.020	0.024
C8	0.037	0.015	-0.004	0.005	0.045	0.016	-0.001	0.018

na, Data not available.

In (2) and (3), C_1 is a unit conversion factor (10^{-3} L cm^{-3}), R is the gas constant (8.314 J mol^{-1} K^{-1}), and the superscripts "b" and "p" have the same meaning as in (1). Errors in Y_{SO_4} and Y_{NO_3} (Table 1) result from uncertainties in the measurements of [SO_4^{2-}] (±8%), [NO_3^-] (±8%), and L^p_{EMO} and L^b_{EMO} (±8%). Systematic errors in Y_{SO_4} may result if a disproportionate fraction of sulfate oxidation occurs in droplets smaller than 2 μm. Such errors are sensitive to the manner in which *p*H and S(IV) are distributed as a function of droplet size [*Hegg and Larson*, 1990]. Experiments conducted at EMO reveal that small cloud droplets tend to be more acidic than large droplets [*Snider*, 1989]. These observations are consistent with those of *Rancourt and Howe* [1987], *Munger et al.* [1989], and *Levin et al.* [1990]. Hence underestimation of Y_{SO_4} resulting from the inefficient collection of small droplets is not indicated.

The pseudo-first-order SO_2 reaction rate (R_{SO_2}, s^{-1}) was calculated from values of Y_{SO_4}, the background ($X^b_{SO_2}$, ppbv) and plume ($X^p_{SO_2}$, ppbv) SO_2 mixing ratio measurements, and the in-cloud reaction time (t_R, s):

$$R_{SO_2} = Y_{SO_4} / t_R(X^p_{SO_2} - X^b_{SO_2}) \quad (4)$$

R_{SO_2} represents the fractional rate of change of SO_2 mixing ratio due to reactions in cloud.

3.3. Subcloud Measurements and SO_2 Reaction Times

Relative humidity at the PAM-II station was measured using a Rotronix MP-100 probe and converted to dew point temperature (T_{DP}) using the PAM-II dry bulb temperature measurement (T_{PAM}). Independently, T_{DP} was also obtained from psychrometer measurements using a 10% ethanol solution (4.5 °C freezing point depression) on the wet bulb sensor. The two measurements of T_{DP} were in agreement within ±0.5 °C.

The lifted condensation level (LCL) was calculated as

$$LCL = 122(T_{PAM} - T_{DP}) \quad (5)$$

assuming adiabatic ascent. Values of LCL derived from (5) were compared with balloon measurements and an average error of ±12% was obtained. This error is comparable to the uncertainty in LCL resulting from errors in T_{DP}.

The SO_2 reaction time, t_R, was calculated using

$$t_R = t_T (S_2/(S_2 + S_1)) \quad (6)$$

Table 2. Cloud Properties and SO_2 Reaction Times

Date	ID	T_{EMO}, °C	L_{EMO}, cm^3 m^{-3}	L_{PARCEL}, cm^3 m^{-3}	LWC Ratio	t_R, min	σ_{tR}, min
Jan. 29, 1987	52	-13.0	0.054	0.208	0.3	4.8	2.4
	53	-12.0	0.067	na	na	2.0[a]	1.5
Feb. 19, 1988	84	-13.7	0.039	0.038	1.0	3.9	0.8
Feb. 20, 1988	89	-11.3	0.195	0.382	0.5	8.7	1.1
	8B	-10.2	0.141	0.322	0.4	7.8	1.3
	8X	-9.7	0.188	0.335	0.6	7.0	1.2
	94	-10.1	0.177	0.426	0.4	10.0	1.4
Mar. 23, 1988	B1	-5.2	0.046	0.140	0.3	5.0	0.8
Jan. 6, 1989	2E	-17.3	0.089	0.403	0.2	10.0	1.1
	2G	-17.5	0.065	0.406	0.2	11.0	1.1
	2J	-18.4	0.084	0.370	0.2	10.0	0.9
	2L	-19.1	0.065	0.343	0.2	9.4	0.9
	2N	-20.1	0.075[b]	0.315	0.2	9.9	0.9
Jan. 8, 1989	43	-23.4	0.033	0.233	0.1	3.8	0.5
Feb. 26, 1989	66	-6.2	0.329	0.943	0.3	21.0	2.2
Feb. 28, 1989	8D	-11.5	0.077	0.290	0.3	5.6	0.8
	8F	-11.3	0.146	0.420	0.3	5.5	0.7
	8H	-11.2	0.170	0.540	0.3	8.9	0.9
	8J	-11.1	0.062	0.400	0.2	6.7	1.0
Mar. 22, 1989	CX	-6.6	0.090[b]	0.099	0.9	2.0	0.5
	C1	-6.2	0.108	0.162	0.7	2.2	0.3
	C4	-6.0	0.141	0.222	0.6	2.6	0.5
	C6	-5.2	0.148	0.206	0.7	2.8	0.5
	C8	-4.5	0.102[c]	0.074	1.4	1.8	0.5

ID, Identification.
na, Data not available.
[a] Cloud base determined by visual observation.
[b] Averaged Commonwealth Scientific and Industrial Research Organization (CSIRO) probe liquid water content (LWC) measurements.
[c] Measurements were made in a dissipating cloud and cloud base was only ≈50 m lower than EMO.

where S_1 is the distance between the Brush Creek site and cloud base, and S_2 is the distance between cloud base and EMO (as illustrated in Figure 1, both S_1 and S_2 are measured along the Brush Creek drainage). The total transport time, t_T, was taken to be the difference in time between the midpoint of the interval of gas release and the midpoint of the observed plume at EMO. Values of t_T obtained from simultaneous releases of SO_2 and SF_6 agree within 10%. Because of plume dispersion and vertical gradients in the horizontal wind, values of t_T are typically 20% larger than the difference between the start time of a plume release and the initial detection of the plume at EMO. Values of t_R and its uncertainty (σ_{t_R}) are listed in Table 2; σ_{t_R} depends on the error in T_{DP} and the slope of the mountain surface.

4. Observations

4.1. Cloud Properties

Calculated and observed values of LWC, L_{PARCEL} and L_{EMO}, are illustrated in Figures 2 and 3 for two experiments (from February 28, 1989, and from March 22, 1989). Values of L_{PARCEL} were derived using measurements of T_{PAM} and T_{DP}, shifted forward in time by t_T, and assuming adiabatic ascent from the Brush Creek site. Temperature, LWC, and reaction time data are given for all experiments in Table 2. The LWC ratio, L_{EMO}/L_{PARCEL}, was around 0.3 for February 28, 1989, as was most frequently the situation; March 22, 1989, was one of the few days when this ratio was closer to unity. The difference between T_{EMO} and the parcel temperature was less than the uncertainty associated with the measurement of T_{EMO}.

It is evident from Table 2 and from Figures 2 and 3 that the LWC ratios are highly variable and in most cases are 0.5 or lower. Therefore the cloud parcels reaching EMO cannot be considered as adiabatic, closed entities. This finding is consistent with earlier studies at EMO [*Politovich and Vali*, 1983]. Available observations do not provide a definitive explanation for the phenomenon but are most consistent with the proposition that there is some divergence of the airflow around the mountain peak and that the cloud at the EMO is a mixture of air parcels that were lifted differing amounts. Some part of the air has risen directly along the mountain surface some entered the cloud at its leading edge farther upwind. The latter undergo less vertical displacement than the difference between cloud base and EMO altitudes. An additional contribution to the

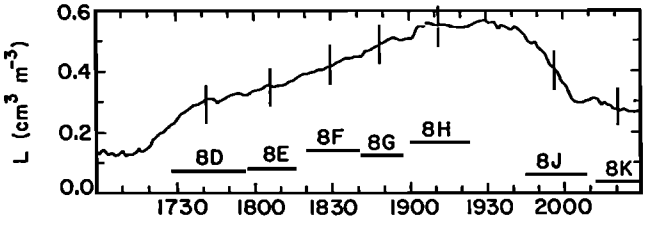

Figure 2. Time series plots of L_{EMO}, averaged over the cloud water collection intervals (indicated by thick horizontal lines), and L_{PARCEL} on February 28, 1989. Uncertainties in L_{PARCEL} are indicated by vertical lines coincident with the midpoint of each cloud water collection interval.

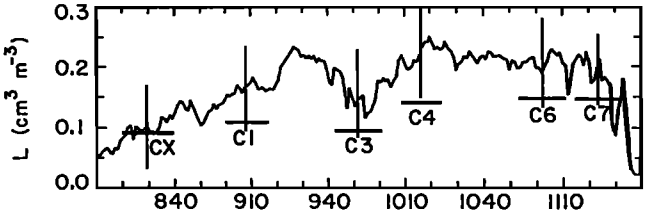

Figure 3. Time series plots of L_{EMO}, averaged over the cloud water collection intervals (indicated by thick horizontal lines), and L_{PARCEL} on March 22, 1989. Uncertainties in L_{PARCEL} are indicated by vertical lines coincident with the midpoint of each cloud water collection interval. Commonwealth Scientific and Industrial Research (CSIRO) probe measured liquid water content (LWC) was averaged over the interval labeled CX.

reduction of LWC comes from the loss of vapor to the snow-covered mountain surface. A third factor is the removal of cloud droplets by riming onto trees. Some of the water content is converted to ice crystals, but this is known to be negligibly small in most cases. We are unable to provide quantitative evaluations of these contributing factors. Cloud top entrainment is expected to have minimal effects because cloud parcels are negatively buoyant at cloud top with respect to the environment and because EMO is closer in altitude to cloud base than to cloud top.

The fact that mixing and fluctuations in the airflow are present is evident in the short-term variability of the released gases SF_6 and SO_2 observed at EMO (see Figures 4 and 5). Although our field measurements are based on averages over cloud water sampling intervals which are longer than the fluctuations observed at EMO, this compensation is incomplete because of SO_2 dilution and the replenishment of H_2O_2. We examine the possible consequences of these processes in section 8.

4.2. Chemical Measurements

The gas phase measurements of SF_6 (X_{SF6}, ppbv), SO_2, H_2O_2, and sulfate dissolved in cloud water ($X_{SO_4} = 10^9 L_{EMO}[SO_4^{2-}]C_1RT_{EMO}/P_{EMO}$, ppbv), obtained on February 28, 1989 and March 22, 1989, are illustrated in Figures 4 and 5. When SF_6 and SO_2 were released coincidentally, a strong correlation between the two time series is evident. These correlated measurements substantiate the assertion that background SO_2 mixing ratios vary insignificantly over the time interval required for analyzing both plume and background conditions.

Five-minute zeroing intervals for SO_2 and H_2O_2 are seen to bracket the plume intervals and to interrupt one of the plume intervals on March 22, 1989 (Figure 5). Decreases in H_2O_2 mixing ratio and increases in sulfate are evident during all of the plume intervals. The largest decreases in H_2O_2 (0.15 ppbv at ≈1732 MST (Figure 4) and 0.13 ppbv at ≈0826 MST (Figure 5)) are coincident with the largest instantaneous values of SO_2 mixing ratio (2.5 and 2.0 ppbv in Figures 4 and 5, respectively). Many of the cloud water sampling intervals overlap periods corresponding to both plume and background conditions, and therefore derived values of $D_{H_2O_2}$ are considerably smaller than the largest instantaneous decreases in H_2O_2. The overlaps result from

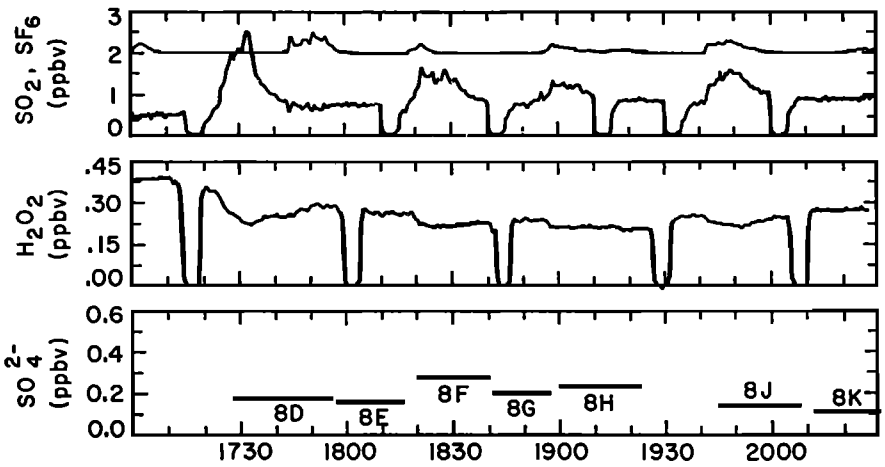

Figure 4. Time series plots of X_{SO_2} (top, thick line); X_{SF_6} (top, thin line); $X_{H_2O_2}$ (middle); and X_{SO_4} (bottom, thick horizontal lines) from February 28, 1989.

unexpected variations in t_T, and from rapid SO_2 increases early in the plume intervals. These factors, combined with the requirement of collecting rime samples of sufficient sizes for chemical analyses, hinder accurate coordination of SO_2 release and rime collection intervals.

The extent of reaction between H_2O_2 and SO_2 and between SO_2 and other reactants can be estimated from the values of $D_{H_2O_2}$ and Y_{SO_4} plotted in Figure 6 and from the values of $D_{H_2O_2}$, Y_{SO_4}, and D_{ORGA} summarized in Table 1. We have made the assumption that nitrate mixing ratios remain constant over the sampling intervals corresponding to background and plume measurements. Therefore nonzero values of Y_{NO_3} are expected to result from measurement errors and not from systematic variations in the amount of nitrate precursor (either nitric acid or aerosol nitrate) entering the cloud. This assumption appears valid for all but four (52, 8B, 8F, and 8J) of the experiments. Because of the steady state assumption required to calculate Y_{SO_4}, these experiments were excluded from the following analysis.

Omission of data values corresponding to experiments 8B, 8F, and 8J (a value of $D_{H_2O_2}$ is not available for experiment 52), the results of experiments 94 and 66, which correspond to the largest observed values of $D_{H_2O_2}$ and Y_{SO_4}, and the results of experiment 84 which is associated with a negative value of Y_{SO_4}, enables the observed values of $D_{H_2O_2}$ and Y_{SO_4} to be related by the expression $Y_{SO_4} = 1.21(\pm 0.13)D_{H_2O_2}$. If results of experiments 94, 66, and 84 are not omitted from the data set, the relationship is $Y_{SO_4} = 0.93(\pm 0.05)D_{H_2O_2}$. The fact that the ratio $D_{H_2O_2}/Y_{SO_4}$ is nearly unity suggests that H_2O_2 is the dominant S(IV) oxidant. This conclusion is supported by the fact that the absolute values of D_{ORGA} are generally less than the corresponding uncertainties. Furthermore, depletions of ozone were not detected. However, the precision of the ozone monitor is not sufficient for quantifying changes in ozone mixing ratio (X_{O_3}, ppbv) less than 1 ppbv. As ozone or molecular oxygen depletions comparable to Y_{SO_4} cannot be excluded by measurement, a cloud chemistry model, initialized with gas and aqueous measurements made at EMO, is used to assess the potential importance of the various SO_2 reaction pathways.

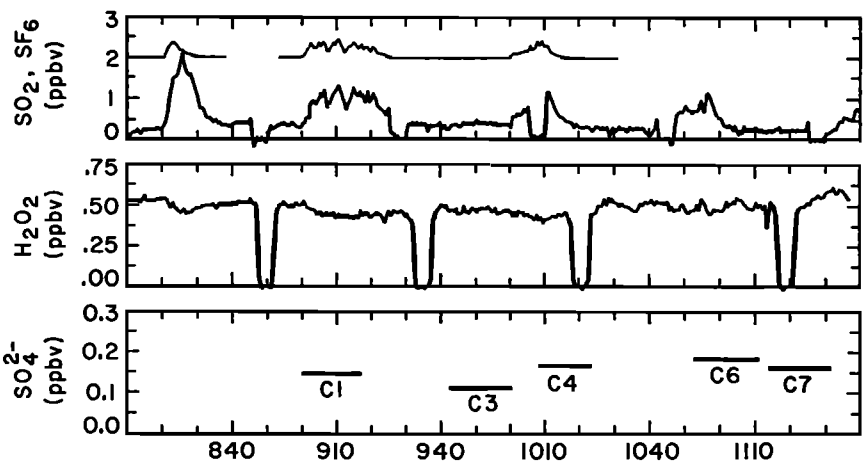

Figure 5. Time series plots of X_{XO_2} (top, thick line); X_{SF_6} (top, thin line); $X_{H_2O_2}$ (middle); and X_{SO_4} (bottom, thick horizontal lines) from March 22, 1989.

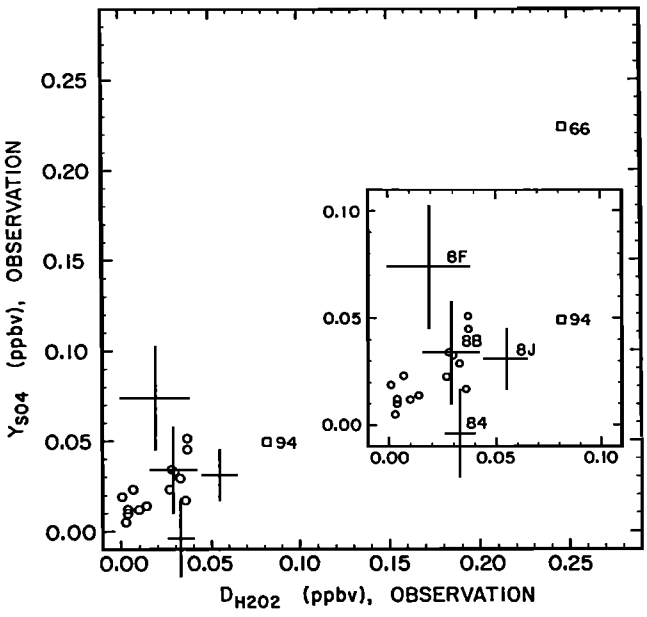

Figure 6. Comparison of observed H_2O_2 depletions ($D_{H_2O_2}$, abscissa) and observed sulfate yields (Y_{SO_4}, ordinate). Errors associated with experiments 84, 8B, 8F, and 8J are indicated and data values from these experiments are labeled in the inset figure. Data values corresponding to experiments 94 and 66 are also labeled. The slope of the best fit line, forced through the origin, and calculated using only those data values indicated by circles is 1.21 (±0.13).

5. Model Description

5.1. Description of Three Models

Table 3 identifies the three models used in the following analysis and the principal capabilities and limitations of each. An assumption common to all of the calculations is that the in-cloud reaction temperature is equal to T_{EMO}. Values of R_{SO_2} calculated using the pseudo-first-order model and values of $D_{H_2O_2}$ calculated using the analytic model are compared with field observations in sections 7.1 and 8.1, respectively. The analytic and the pseudo-first-order models, described in the Appendix, are predicated on the assumption that S(IV) is oxidized by only one coreactant.

The numerical model calculates the time evolution of the activities and concentrations of 26 aqueous phase species and the mixing ratios of 10 gas phase species. It is assumed that cloud water composition at any instant in time is uniform over a population of monodisperse droplets. The numerical model and the measurements that are used to initialize it are discussed below.

5.2. Model Initialization and Input Data

Numerical model simulations of background conditions are initialized with EMO measurements obtained during background cloud water collection intervals. With the exception of the value of SO_2 mixing ratio, simulations of plume-SO_2 conditions are also initialized with background measurements. Model-predicted quantities consist of the total S(IV) coreactant depletions and the total sulfate yields, both equal to the sum of that due to in-cloud reaction and reaction subsequent to rime collection. Values of Y_{SO_4}, $D_{H_2O_2}$, D_{ORGA}, ozone depletion (D_{O_3}, ppbv), formaldehyde depletion (D_{HCHO}, ppbv), and the depletion of molecular oxygen (D_{O_2}, ppbv) resulting from in-cloud reaction were calculated as the difference between the extent of reaction corresponding to paired simulations of plume-SO_2 and background conditions evaluated at model simulation time (t, s) = t_R. The calculations of yields and depletions subsequent to rime sample collection are discussed in section 6.

Chemical data used for each run of the numerical model are shown in Table 4. Nonvolatile components (i.e., SO_4^{2-}, Cl^-, the base cations (Ca^{2+}, Mg^{2+}, Na^+), and the trace metals (Fe(III) and Mn(II))) are assumed to be constituents of an internally mixed and monodisperse aerosol. This aerosol, consisting of the base cations (mixing ratio X_M, ppbv), sulfate (mixing ratio $X_{AB} + X_S$, ppbv), and chloride (mixing ratio X_{CL}, ppbv), is dissolved in the cloud water at cloud base. Measurements of L^b_{EMO}, $[NH_4^+]$, and $[SO_4^{2-}]$ were used to derive the mixing ratio of aerosol ammonium bisulfate (X_{AB}, ppbv). Any excess sulfate was combined with protons forming a sulfuric acid (mixing ratio X_S, ppbv) component of the aerosol. Values of the initial ammonia mixing ratio (X_{NH_3}, ppbv) range between 0.0 ppbv (i.e., samples containing an excess of cloud water sulfate relative to the ammonia species) and 0.3 ppbv. Ammonia and the nitric and formic acids were initialized as gas phase species. The initial nitric acid mixing ratio (X_{HNO_3}, ppbv) was calculated as $10^9 L^b_{EMO}[NO_3^-]C_1RT_{EMO}/P_{EMO}$. The initial formic acid mixing ratio (X_{HCO_2H}, ppbv) was calculated from *p*H and aqueous formic acid species measurements assuming Henry's law of equilibrium between the cloud water and the interstitial HCO_2H. Other model inputs include the values of t_R and T_{EMO} (see Table 1) and the values of L^b_{EMO}, $X_{Mg} = 10^9 L^b_{EMO}[Mg^{2+}]C_1RT_{EMO}/P_{EMO}$ (ppbv), $X^p_{SO_2}$, $X^b_{SO_2}$, $X^b_{H_2O_2}$, X_{O_3}, and the organohydroperoxide mixing ratio (X_{ORGA}, assumed equivalent to methyl hydroperoxide), all summarized in Table 4. The initial

Table 3. Summary of Models

Model Type	Reagent Depletion?	LWC	$[H^+]$	Ionic Strength	No. of Reaction Pathways	Temperature and Pressure
Pseudo-first-order	no	constant	constant	constant	1	constant
Analytic	yes	equation (7)	constant	constant	1	constant
Numerical	yes	equation (7)	variable	variable	5	constant

Table 4. Model Input Data

ID[a]	T_{EMO}, °C	L_{EMO}, $cm^3\ m^{-3}$	X_{Mg}, ppbv	X_M, ppbv	$2X_S + X_{Cl} + X_{AB}$, ppbv	X_{NH_3}, ppbv	X_{HNO_3}, ppbv	X_{HCO_2H}, ppbv	X_{SO_2}[b], ppbv	$X_{H_2O_2}$, ppbv	X_{ORGA}, ppbv	X_{O_3}[c], ppbv
84/83	-13.7	0.045	0.02	0.19	0.18	0.00	0.23	0.10	2.4 / 1.3	0.120	0.054	36.
89/88	-11.8	0.182	0.02	0.19	0.20	0.30	0.30	0.10	1.0 / 0.6	0.159	0.108	36.
8X/8C	-9.2	0.231	0.02	0.16	0.28	0.29	0.42	0.10	1.0 / 0.6	0.192	0.087	36.
94/93	-10.2	0.177	0.01	0.19	0.37	0.21	0.43	0.10	2.0 / 0.5	0.232	0.095	36.
B1/B0	-5.6	0.066	0.05	0.59	0.94	0.00	0.09	0.15	0.8 / 0.2	0.310	0.100	36.
2E/2I	-17.8	0.053	0.02	0.28	0.19	0.00	0.11	0.05	1.2 / 0.9	0.036	0.015	30.
2G/2I	-17.8	0.053	0.02	0.28	0.19	0.00	0.11	0.05	1.4 / 0.9	0.036	0.015	30.
2J/2K	-18.7	0.078	0.03	0.36	0.21	0.00	0.15	0.05	2.8 / 1.3	0.028	0.017	27.
2L/2K	-18.7	0.078	0.03	0.36	0.21	0.00	0.15	0.05	2.0 / 1.3	0.028	0.017	27.
2N/2P	-21.0	0.071	0.03	0.33	0.30	0.00	0.34	0.05	2.1 / 1.5	0.027	0.014	27.
43/41	-23.6	0.035	<0.01	0.05	0.06	0.00	0.04	0.03	0.9 / 0.5	0.052	0.022	34.
66/65	-6.3	0.296	0.01	0.08	0.50	0.00	0.10	0.04	1.1 / 0.4	0.672	0.144	33.
8D/8E	-11.3	0.087	0.01	0.13	0.45	0.07	0.31	0.28	1.1 / 0.8	0.344	0.068	44.
8H/8G	-11.3	0.127	0.01	0.14	0.65	0.08	0.45	0.32	1.2 / 0.8	0.327	0.069	44.
CX/CW	-6.2	0.095	0.01	0.09	0.13	0.26	0.19	0.13	0.9 / 0.3	0.673	0.092	35.
C1/C3	-6.2	0.095	0.01	0.09	0.13	0.26	0.19	0.13	1.0 / 0.4	0.539	0.096	35.
C4/C3	-6.2	0.095	0.01	0.09	0.13	0.26	0.19	0.13	0.8 / 0.4	0.539	0.096	35.
C6/C7	-4.7	0.147	0.01	0.13	0.17	0.08	0.15	0.05	0.5 / 0.2	0.625	0.109	35.
C8/C9	-4.4	0.084	<0.01	0.05	0.17	0.09	0.12	0.06	0.6 / 0.2	0.685	0.098	35.

With the exception of SO_2 mixing ratios, all values in this table correspond to the background measurements.

[a] Sample Identifier; the first identifier corresponds to the SO_2-plume sample (see Table 1), the second to the background sample.

[b] Values of both plume (left) and background (right) SO_2 mixing ratios.

[c] Values of ozone mixing ratio prior to sample 2E are Elk Mountain wintertime averages.

formaldehyde mixing ratio (X_{HCHO}) was assumed equal to 0.5 ppbv.

5.3. Thermodynamic and Kinetic Data

The equilibria and rate laws are summarized in Tables 5-7. The Henry's law constants, $K_{H,i}$ (M atm^{-1}) in Table 5, are identified by the subscript i=1 (NH_3) through i=10 (HNO_3). The aqueous phase equilibria (Table 6), applicable to reversible reactions of the dissolved gases, to the S(VI) species (SO_4^{2-} and HSO_4^-), and to the dissolved Fe(III) species ($(Fe(SO_3)OH)^o$, $Fe(SO_3)^+$, $Fe(OH)_2^+$, $Fe(OH)^{2+}$, and Fe^{3+}) are also identified by the subscript "i" (i=11 identifies the acidity constant of bisulfate anion and i=12 identifies the aqueous equilibria corresponding to the Fe(III) species). A second subscript (either A1 or A2, Hy, C1, C2, or S) identifies acidity, hydrolysis, complexation, or solubility equilibrium constants. Irreversible reactions are described in terms of rate laws which are functions of the rate constants, reagent concentrations, and Arrhenius parameters summarized in Table 7. Rate constants (k_{ij}) are identified by two subscripts: "i" identifies the S(IV) coreactant and "j" identifies reactions involving dissolved SO_2 (j=0), HSO_3^- (j=1), SO_3^{2-} (j=2), or the totality of dissolved S(IV) species (j=4). The reaction enthalpies (Tables 5-6) and the Arrhenius parameters (Table 7) are used to compute the temperature dependence of the equilibria and the reaction rate constants using Van't Hoff's equation or transition state theory in the case of the HCHO/S(IV) reaction mechanism.

The rate of the H_2O_2/S(IV) reaction is proportional to the quantity $k_{8,1}K_{H,8}K_{H,2}K_{A1,2}$ (M/(s atm^2)) which increases from 0.46×10^{12} to 3.2×10^{12} over the temperature interval +5 to -15 °C. Values of $k_{8,1}K_{H,8}K_{H,2}K_{A1,2}$ would range from 0.74×10^{12} to 9.5×10^{12}, on the basis of the thermodynamic and kinetic data used by *Chandler et al.* [1989]. Thus for the same coreactant partial pressures, LWC, and temperature, the rate of the H_2O_2/S(IV) reaction predicted here is approximately a factor of 2 smaller than predictions based on laboratory data in the work of *Chandler et al.* [1989].

5.4. Cloud Microphysics

The reaction time, t_R, defines the time over which LWC evolves from a cloud base value (L_{CB}, assumed to be 0.001 $cm^3\ m^{-3}$) and L^b_{EMO}. The assumption is made that the rate of increase of LWC is linear with time. The time evolution of LWC is given by

$$L(t) = L_{CB} + \frac{t\ (L^b_{EMO} - L_{CB})}{t_R} \quad (7)$$

Cloud droplet concentration, n_D, is assumed constant and equal to the average value (n_D = 300 cm^{-3}) reported by *Politovich and Vali* [1983]. The droplet radius is calculated as a function of time from

$$r(t) = \left(\frac{3L(t)}{4\pi n_D}\right)^{1/3} \quad (8)$$

5.5. Speciation of Fe(III) and S(IV)

Dissolved Mn(II) and Fe(III) are the catalysts of the O_2/S(IV) reaction pathway. We have utilized Fe/Mg (1.0) and Mn/Mg (0.018) mole ratios obtained from measurements of Elk Mountain precipitation, consisting of rimed

Table 5. Henry's Law Constants

Symbol	Species	$K_H(298)$, M/atm	$\Delta H(298)$, kJ/mol	Reference
$K_{H,1}$	NH_3	5.9(+1)	-34.2	*Hoffman and Calvert* [1985]
$K_{H,2}$	SO_2	1.2(+0)	-26.3	*Maahs* [1982]
$K_{H,3}$	CO_2	3.4(-2)	-20.3	*Hoffmann and Calvert* [1985]
$K_{H,4}$	HCO_2H	5.6(+3)	-47.4	*Keene and Galloway* [1986]
$K_{H,5}$	HCHO	3.5(+0)	-20.1	*Hoffmann and Calvert* [1985], *Bell* [1966]
$K_{H,6}$	O_3	1.1(-2)	-21.3	*Chameides* [1984]
$K_{H,7}$	O_2	1.2(-3)	-15.0	*Hoffmann and Calvert* [1985]
$K_{H,8}$	H_2O_2	7.4(+4)	-55.0	*Lind and Kok* [1986]
$K_{H,9}$	CH_3O_2H	2.2(+2)	-46.6	*Lind and Kok* [1986]
$K_{H,10}$	HNO_3[a]	2.6(+6)	-72.3	*Chameides* [1984]

Read 5.9(+1) as $5.9\times10^{+1}$.
[a] Corresponds to the reaction $HNO_{3(g)} \rightarrow H^+_{(aq)} + NO_{3(aq)}^-$; the units of $K_{H,10}$ are M^2atm^{-1}.

Table 6. Aqueous Equilibria

Symbol	Reaction	K (298), M^n	ΔH(298), kJ/mol	Reference
$K_{B1,1}$	$NH_3 + H_2O = NH_4^+ + OH^-$	1.7(-5)	+ 3.77	*Hoffmann and Calvert* [1985]
$K_{A1,2}$	$SO_2 + H_2O = HSO_3^- + H^+$	1.3(-2)	- 16.3	*Maahs* [1982]
$K_{A2,2}$	$HSO_3^- = SO_3^{2-} + H^+$	6.4(-8)	- 11.9	*Maahs* [1982]
$K_{A1,3}$	$CO_2 + H_2O = HCO_3^- + H^+$	4.5(-7)	+ 7.66	*Drever* [1988]
$K_{A1,4}$	$HCO_2H = HCO_2^- + H^+$	1.8(-4)	+ 2.13	*Weast* [1982]
$K_{Hy,5}$	$HCHO + H_2O = H_2C(OH)_2$	1.3(+3)	- 33.6	*Hoffmann and Calvert* [1985], *Bell* [1966]
$K_{A2,11}$	$HSO_4^- = SO_4^{2-} + H^+$	1.0(-2)	- 22.6	*Hoffmann and Calvert* [1985]
$K_{A1,12}$	$Fe^{3+} + H_2O = FeOH^{2+} + H^+$	6.1(-4)	+ 43.6	*Drever* [1988]
$K_{A2,12}$	$Fe^{3+} + 2H_2O = Fe(OH)_2^+ + 2H^+$	6.2(-9)	+100	*Drever* [1988]
$K_{C1,12}$	$Fe^{3+} + SO_3^{2-} = FeSO_3^+$	2.8(+8)[a]	0.	*Conklin and Hoffmann* [1988], *Jacob et al.* [1989]
$K_{C2.12}$	$Fe(OH)^{2+} + SO_3^{2-} = Fe(OH)(SO_3)^0$	3.4(+8)[a]	0.	*Conklin and Hoffmann* [1988], *Jacob et al.* [1989]
$K_{S,12}$	$Fe(OH)_{3(s)} + 3H^+ = Fe^{3+} 3H_2O$	6.8(+4)	- 83.1	*Drever* [1988]
K_W	$H_2O = OH^- + H^+$	1.0(-14)	+ 55.8	*Hoffmann and Calvert* [1985]

Read 1.7(-5) as 1.7×10^{-5}.

[a] Adjusted to zero ionic strength using Davies approximation.

Table 7. Rate Laws and Rate Constants

Reaction	$k_{i,j}$ (298), $M^n\ s^{-1}$	E_a, kJ/mol	Reference
$-\frac{d[S(IV)_1]}{dt} = k_{5,1}\,[HCHO][HSO_3^-]$	3.8(+2)	$\Delta H^{\neq} = 22.1\ kJ\ mol^{-1}$ $\Delta S^{\neq} = -121.\ J\ mol^{-1}\ K^{-1}$	*Boyce and Hoffmann* [1984]
$-\frac{d[S(IV)_2]}{dt} = k_{5,2}\,[HCHO][SO_3^{2-}]$	1.0(+7)	$\Delta H^{\neq} = 21.0\ kJ\ mol^{-1}$ $\Delta S^{\neq} = -40.2\ J\ mol^{-1}\ K^{-1}$	*Boyce and Hoffmann* [1984]
$-\frac{d[S(IV)_0]}{dt} = k_{6,0}\,[O_3][SO_2]$	2.4(+4)	0.	*Hoffmann* [1986]
$-\frac{d[S(IV)_1]}{dt} = k_{6,1}\,[O_3][HSO_3^-]$	3.7(+5)	46.0	*Hoffmann* [1986]
$-\frac{d[S(IV)_2]}{dt} = k_{6,2}\,[O_3][SO_3^{2-}]$	1.5(+9)	43.9	*Hoffmann* [1986]
$-\frac{d[S(IV)_4]}{dt} = k_{7,4}\,[Mn(II)][Fe(III)]_T[H^+]^{0.67}[S(IV)]_T$ (pH>4.2)	2.5(+13)	70.1	*Ibusuki and Takeuchi* [1987]
$-\frac{d[S(IV)_4]}{dt} = k_{7,4}\,[Mn(II)][Fe(III)]_T[H^+]^{-0.74}[S(IV)]_T$ (pH<4.2)	3.7(+7)	70.1	*Ibusuki and Takeuchi* [1987]
$-\frac{d[S(IV)_1]}{dt} = \frac{k_{8,1}\,[H^+][HSO_3^-][H_2O_2]}{(1.+\ 13.[H^+])}$	7.4(+7)	39.5	*Hoffmann and Calvert* [1985]
$-\frac{d[S(IV)_1]}{dt} = k_{9,1}\,[H^+][HSO_3^-][CH_3O_2H]$	1.7(+7)	31.6	*Lind et al.* [1987]

Read 3.8(+2) as $3.8 \times 10^{+2}$.

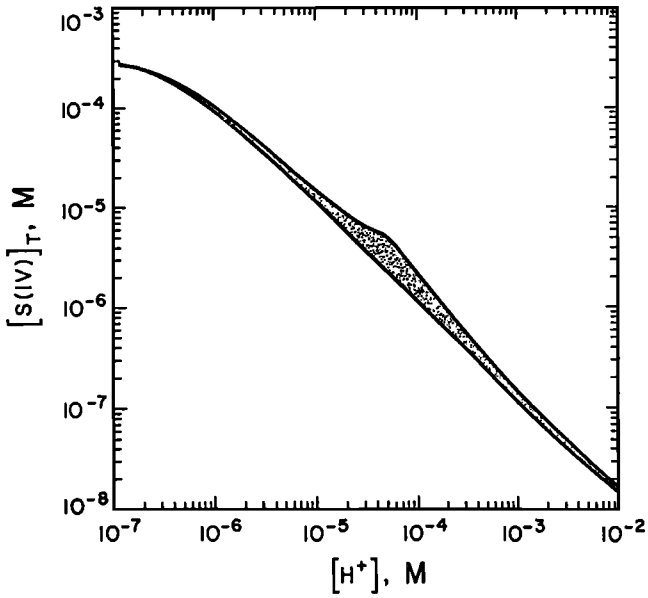

Figure 7a. $[S(IV)]_T$ in the equilibrium system $SO_{2(g)}/Fe(OH)_{3(s)}/H_2O$ as a function of hydrogen ion concentration. Ionic strength = 10^{-2} M, T = 263 K, X_{Mg} = 0.015 ppbv, Fe/Mg mole ratio = 1.0, L = 0.1 cm^3m^{-3}, and X_{SO_2} = 1 ppbv. The lower boundary of the hatched region defines values of $[S(IV)]_T$ corresponding to the $SO_{2(g)}/H_2O$ system. The shaded area defines a region of enhanced values of $[S(IV)]_T$ due to the formation of sulfitoiron(III) complexes.

snow (C. Boutron, personal communication, 1988), and measurements of X_{Mg} to infer the total (i.e., solid and dissolved) amounts of Fe(III) and Mn(II) in the cloud water. The total amount of cloud water Fe(III) (0.004 - 0.049 ppbv) is consistent with measurements of iron associated with submicrometric aerosol particles in the Rocky Mountains [*Lawson and Winchester*, 1978] and over the central United States [*Kim et al.*, 1988]. Apportionment of the total amount of Fe(III) between an assumed amorphous ferric hydroxide solid phase ($Fe(OH)_{3(s)}$) and dissolved Fe(III) is predicted by an equilibrium model (see below). Precipitation of solid $Mn(OH)_{2(s)}$ only occurs at *p*H values > 8, so we also assume that Mn(II) in cloud water is present as the free ion.

The hydrogen ion dependence of the dissolved Fe(III) species concentration, $[Fe(III)]_T$ (i.e., the sum of $[Fe(SO_3)(OH)^0]$, $[Fe(SO_3)^+]$, $[Fe(OH)_2^+]$, $[Fe(OH)^{2+}]$, and $[Fe^{3+}]$), and the dissolved S(IV) species concentration, $[S(IV)]_T$ (i.e., the sum of $[Fe(SO_3)(OH)^0]$, $[Fe(SO_3)^+]$, $[SO_3^{2-}]$, $[HSO_3^-]$, and $[SO_2]$), are plotted in Figures 7a and 7b. Comparisons are also made to the systems $SO_{2(g)}/H_2O$ and $Fe(OH)_{3(s)}/H_2O$. At hydrogen ion concentrations less than $\approx 7 \times 10^{-5}$ M, large enhancements of $[Fe(III)]_T$ and smaller enhancements of $[S(IV)]_T$ result due to the formation of $Fe(SO_3)(OH)^0$ and $Fe(SO_3)^+$. Because we assume that all soluble Fe(III) complexes have similar reactivities and that values of $[Fe(III)]_T$ are under equilibrium control, the rate of the O_2/S(IV) oxidation pathway, dependent on $[Fe(III)]_T$ and $[S(IV)]_T$, is accelerated by the formation of the sulfitoiron(III) complexes.

5.6. Ionic Strength

For the dilute solutions of interest to this study (even droplets at cloud base contain solute concentrations less than 1 M) the Davies approximation [*Stumm and Morgan*, 1970] is used to account for differences between ion activity and ion concentration. Typical ionic strengths in cloud water samples collected at EMO indicate appreciable (i.e., > 10%) deviations from ideality in the case of trivalent Fe^{3+}. A much more pronounced deviation between ion activity and concentration is predicted for samples traced back to the value of LWC (0.001 cm^3 m^{-3}) corresponding to model conditions at cloud base.

5.7. Numerical Technique

The reaction rate laws have the general form

$$\frac{d[S(IV)_j]}{dt} = -k_j[S(IV)_j][A_i] \qquad (9)$$

where $[A_i]$ symbolizes the concentration of coreactant, $[S(IV)_j]$ identifies a particular S(IV) species, and the second-order rate coefficient (k_j) is a function of the rate constants given in Table 7 and other quantities (i.e., T_{EMO}, $[H^+]$, etc.).

The rate laws were integrated using a finite difference scheme

$$X_{i,t+\delta t} = X_{i,t} + \frac{\delta t L(t) R T_{EMO} C_1}{P_{EMO}} \sum_{j=1}^{j=4} \frac{d[S(IV)_j]}{dt} \qquad (10)$$

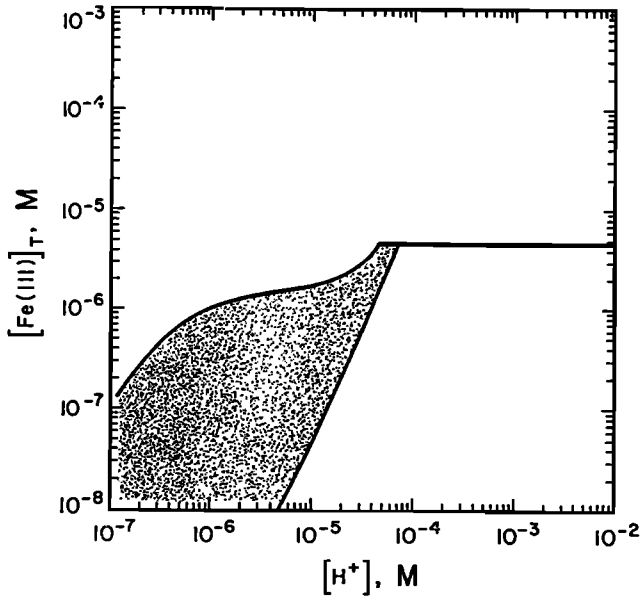

Figure 7b. Total dissolved Fe(III), $[Fe(III)]_T$, in the equilibrium system $SO_{2(g)}/Fe(OH)_{3(s)}/H_2O$ as a function of hydrogen ion concentration. Ionic strength = 10^{-2} M, T = 263 K, X_{Mg} = 0.015 ppbv, Fe/Mg mole ratio = 1.0, L = 0.1 cm^3m^{-3}, and X_{SO_2} = 1 ppbv. The lower boundary of the hatched region defines values of $[Fe(III)]_T$ corresponding to the $Fe(OH)_{3(s)}/H_2O$ system. The shaded area defines a region of enhanced values of $[Fe(III)]_T$ due to the formation of sulfitoiron(III) complexes.

where δt is the time step (0.02 s) and $X_{i,t}$ is the time-dependent total mixing ratio of S(IV) coreactant. The time-dependent mixing ratios of SO_2 (X_{SO_2}) and the S(VI) species resulting from aqueous SO_2 oxidation (X_{SVI}) were calculated using (11) and (12).

$$X_{SVI,t+\delta t}=X_{SVI,t}-\frac{\delta t L(t) RT_{EMO} C_l}{P_{EMO}} \sum_{i=6}^{i=10} \sum_{j=1}^{j=4} \nu_i \frac{d[S(IV)_j]}{dt} \quad (11)$$

$$X_{SO_2,t+\delta t}=X_{SO_2,t}+\frac{\delta t L(t) RT_{EMO} C_l}{P_{EMO}} \sum_{i=5}^{i=10} \sum_{j=1}^{j=4} \nu_i \frac{d[S(IV)]_j]}{dt} \quad (12)$$

In (11) and (12), ν_i is a stoichiometric coefficient that is equal to unity for all of the reaction pathways except the O_2/S(IV) reaction ($\nu_7 = 2$). The different ranges of the summation variable "i" in (11) and (12) reflect the fact that the HCHO/S(IV) pathway does not produce S(VI).

5.8. Gas-to-Droplet Mass Transfer

The fluxes of gaseous HNO_3 and NH_3 to the cloud droplets were calculated using a finite difference form of the Fuchs-Sutugin mass transport equation [*Fuchs and Sutugin*, 1971]. Values of the accommodation coefficient for both HNO_3 and NH_3 were set at 0.01 [*Kirchner et al.*, 1990]. A HNO_3/NH_3 accommodation coefficient of 0.3 [*Van Doren et al.*, 1990] was found to have little or no effect on the results presented here. All other gases were assumed to be in Henry's law equilibrium with the cloud droplets.

5.9. Calculation of $[H^+]$ and Buffering Intensities

Newton's Method was used to calculate $[H^+]$. The charge-balance equation has the following form:

$$\begin{aligned} f([H^+]) = 0.0 &= [H^+] + 3[Fe^{3+}] + 2[Fe(OH)^{2+}] \\ &+ [Fe(OH)_2^+] + [Fe(SO_3)^+] + [M^+] + [NH_4^+] \\ &- 2[SO_4^{2-}] - [HSO_4^-] - [Cl^-] - [HSO_3^-] \\ &- 2[SO_3^{2-}] - [HCO_2^-] - [NO_3^-] - [HCO_3^-] \end{aligned} \quad (13)$$

The numerical algorithm calculates the hydrogen ion concentration and solution ionic strength at each time step. This process is simplified by the fact that several of the terms in (13) (i.e., $[NH_4^+]$, $[HSO_4^-]$, $[SO_4^{2-}]$, $[HCO_2^-]$, $[HCO_3^-]$, and $[NO_3^-]$) can be calculated as functions of $[H^+]$ and by the fact that the concentrations of the base cations ($[M^+] = 2[Ca^{2+}] + 2[Mg^{2+}] + [Na^+]$) and $[Cl^-]$ are only functions of L(t) and the composition of the aerosol used to initialize the model. However, the S(IV) and Fe(III) species are related through the Fe(III) complexation equilibria and therefore the concentrations of these species were evaluated by iterative estimations of the gas/aqueous partitioning of S(IV) and the solution/solid phase partitioning of Fe(III).

As summarized in Table 8, H^+, formic acid, S(IV), and Fe(III) are the dominant buffers of Elk Mountain cloud water *p*H. Buffering intensity resulting from the presence of hydrogen ion and the formic acid species was calculated using (14) and (15)

$$\beta_0 = \text{buffering intensity resulting from } [H^+] = \frac{2.303[H^+]}{\gamma_1} \quad (14)$$

$$\beta_4 = \text{buffering intensity due to formic acid species} = \frac{2.303[HCO_2^-](1.-F)}{\gamma_1} \quad (15)$$

where

$$F = [HCO_2^-]L(t)RT_{EMO}C_l/(10^{-9}X_{HCO2H}P_{EMO})$$

and where γ_1 symbolizes the activity coefficient corresponding to a monovalent ion. Buffering due to the formic acid species is a maximum at *p*H values which are larger than the pK_A of formic acid (3.8 at 263 K) and less than the *p*H values corresponding to efficient partitioning of gaseous formic acid into the aqueous phase. Buffering due to the Fe(III) and S(IV) species cannot be calculated analytically and was therefore evaluated by numerically differentiating the concentrations of dissolved Fe(III) and S(IV) with respect to $[H^+]$.

6. Model Results

Model-predicted values for key quantities are summarized in Table 8. Two values of $[H^+]$ are given, one derived from measurements of cloud water *p*H and another based on the numerical model. In-cloud depletions of H_2O_2 are derived using both the analytic and the numerical models, while the in-cloud depletions of both O_3 and O_2 and the in-cloud sulfate yield are based on the numerical model. The last three columns present the values of sulfate yield and the depletions of both H_2O_2 and O_2 which are predicted by the numerical model to occur subsequent to sample collection, due to the presence of reactants dissolved in the cloud water. Values of D_{HCHO} and D_{ORGA} derived from the numerical model are less than 0.001 ppbv. These values are not shown in Table 8.

The predicted values of $[H^+]$ for $t = t_R$ are in reasonable agreement with those observed. Disparities arise mainly from measurement errors in the anion and cation concentrations used to initialize the numerical model.

Values of $D_{H_2O_2}$ derived from the analytic model are 0.001 to 0.006 ppbv lower than the predictions of the numerical model. The sign of this difference is consistent with the fact that the analytic model does not account for the enhanced concentration of bisulfite ion due to the large values of ionic strength near cloud base. If ionic strength is set to a constant value less than 10^{-4} M, independent of LWC, the differences between the analytic and numerical model predictions of $D_{H_2O_2}$ are less than 0.001 ppbv.

The kinetics of aqueous S(IV) oxidation is sufficiently rapid, and there is excess H_2O_2 (above stoichiometric) in most Elk Mountain cloud water samples, so that S(IV) is fully converted to SO_4^{2-} prior to addition of the hydroperoxide reagent [*Snider et al.*, 1992]. Therefore the measurements of $D_{H_2O_2}$ and Y_{SO_4} become biased by reaction subsequent to rime collection. We accounted for this bias by calculating the values shown in the last three columns of

Table 8. Predictions of the Analytic and Numerical Models

ID	Derived From *p*H $[H^+]$, μM	Numerical Model $[H^+]$, μM	Numerical Model Dominant Buffers	Analytic Model in-Cloud Reaction $D_{H_2O_2}$, ppbv	Numerical Model in-Cloud Reaction				Numerical Model Postcollection Reaction		
					Y_{SO_4}, ppbv	$D_{H_2O_2}$, ppbv	D_{O_3}, ppbv	D_{O_2}[a], ppbv	Y_{SO_4}, ppbv	$D_{H_2O_2}$, ppbv	D_{O_2}, ppbv
84	na	178	H^+, Fe(III)	0.012	0.017	0.013	0.000	0.002	0.002	0.000	0.001
89	na	31	H^+, S(IV)	0.016	0.018	0.017	0.001	0.000	0.008	0.001	0.003
8X	54	52	H^+	0.017	0.019	0.018	0.000	0.000	0.006	0.006	0.000
94	89	117	H^+	0.087	0.091	0.090	0.000	0.000	0.010	0.010	0.000
B1	na	178	H^+	0.018	0.025	0.020	0.000	0.002	0.002	0.002	0.000
2E	na	71	S(IV)	0.002	0.009	0.002	0.000	0.003	0.000	0.000	0.000
2G	na	82	S(IV)	0.004	0.015	0.005	0.000	0.005	0.001	-0.001	0.001
2J	158	92	S(IV)	0.008	0.031	0.008	-0.004	0.013	0.007	-0.002	0.004
2L	na	76	S(IV)	0.004	0.017	0.005	-0.002	0.007	0.004	-0.001	0.002
2N	na	170	H^+, Fe(III)	0.003	0.010	0.003	0.000	0.004	0.003	0.000	0.002
43	na	68	H^+	0.003	0.004	0.003	0.000	0.000	0.002	0.000	0.001
66	63	123	H^+	0.196	0.202	0.202	0.000	0.000	0.003	0.003	0.000
8D	251	241	H^+	0.019	0.020	0.020	0.000	0.000	0.001	0.001	0.000
8H	224	262	H^+	0.025	0.027	0.027	0.000	0.000	0.001	0.001	0.000
CX	na	27	H^+, HCO_2H	0.021	0.022	0.022	0.000	0.000	0.006	0.006	0.000
C1	44	27	H^+, HCO_2H	0.017	0.019	0.018	0.000	0.000	0.006	0.006	0.000
C4	27	27	H^+, HCO_2H	0.014	0.015	0.015	0.000	0.000	0.004	0.004	0.000
C6	32	36	H^+, Fe(III)	0.012	0.013	0.013	0.000	0.000	0.003	0.003	0.000
C8	44	49	H^+, Fe(III)	0.011	0.011	0.011	0.000	0.000	0.003	0.003	0.000

[a] Because of the stoichiometric relationship, $0.5O_2 + SO_3^{2-} \rightarrow SO_4^{2-}$, O_2 contributes an amount $2D_{O_2}$ to the sulfate yield.

Table 8 from numerical model predictions of $[S(IV)]_T$ and $[H_2O_2]$, at $t = t_R$, and using the empirically determined relationship between the H_2O_2 retention coefficient and the droplet impact time [*Snider et al.*, 1992]. However, this approach is complicated by the fact that actual values of $[S(IV)]_T$ are enhanced relative to equilibrium predictions based on measurements of X_{SO_2} and bulk cloud water *p*H [*Perdue and Beck*, 1988]. S(IV) enhancement ratios ranging between 1 and 5 are predicted by *Pandis and Seinfeld* [1991], depending on *p*H values in droplets of differing sizes. Average enhancements equal to 5 were reported at Great Dun Fell in northern England [*Radojevic et al.*, 1990]. As a result, our estimates of Y_{SO_4} for the postcollection reactions may be low, but this error is compensated to some degree by the volatilization of S(IV) species during riming [*Lamb and Blumenstein*, 1987; *Iribarne et al.*, 1990]. Therefore we have not accounted for inefficient retention of the S(IV) species in our calculations of Y_{SO_4}, $D_{H_2O_2}$, and D_{O_3} for reactions subsequent to cloud water collection.

Total oxidant depletion is the sum of the in-cloud depletions and of those subsequent to cloud water collection. For all cases the absolute value of $D_{H_2O_2}$ for the reaction subsequent to cloud water collection is less than 35% of the values of $D_{H_2O_2}$ which result from in-cloud reaction. The extent of postcollection S(IV) oxidation for the H_2O_2-limited samples 84, 89, 2G, 2J, 2L, 2N, and 43 was calculated by first consuming all H_2O_2 by reaction with S(IV) and then allowing O_2 to serve as the final S(IV) oxidant. A subset of these simulations are associated with negative values of $D_{H_2O_2}$ subsequent to sample collection. These values result because $[H_2O_2](t = t_R)$ is predicted to be larger in the background cloud water sample. The negative values of in-cloud D_{O_3} associated with experiments 2J and 2L result from higher *p*H values early in the background simulation and therefore larger rates of reaction via the O_3/S(IV) pathway.

Based on the numerical model, H_2O_2 is predicted to be the dominant S(IV) oxidant in all cases except 2E, 2G, 2J, 2L, and 2N (all conducted on January 6, 1989). For these cases the model predicts total sulfate yields from the O_2/S(IV) pathway that range between 0.006 and 0.034 ppbv and total H_2O_2 depletions of 0.002-0.007 ppbv.

7. Comparison of Model Results With Observations

7.1. Pseudo-First-Order Model

Pseudo-first-order model predictions of the correlative relationships between R_{SO_2} and the independent measurements of oxidant mixing ratio, temperature, LWC, and cloud water composition are discussed in the Appendix. Support was found for the hypothesis that H_2O_2 is the dominant S(IV) oxidant in the positive correlations between R_{SO_2} and $X^b_{H_2O_2}$ ($r=0.85$, $n=17$, $P>0.99$, where P is the confidence level associated with the correlation coefficient), between R_{SO_2} and background measurements of $[H_2O_2]$ ($r=0.63$, $n=17$, $P>0.99$), and in the absence of a significant correlation between R_{SO_2} and L^b_{EMO} ($r=0.07$, $n=18$, $P=0.61$). The lack of a significant correlation between R_{SO_2} and X_{O_3} ($r=0.27$, $n=13$, $P=0.81$) and the lack of a significant inverse correlation between R_{SO_2} and background measurements of $[H^+]$ ($r=-0.44$, $n=11$, $P=0.91$) both argue against the importance of the O_3/S(IV) reaction in wintertime clouds at Elk Mountain. The positive correlation between R_{SO_2} and T_{EMO} ($r=0.68$, $n=18$, $P>0.99$) is not consistent with the kinetics of either the O_3 or the H_2O_2 pathways, although we suspect that it reflects seasonal variations in the abundance of H_2O_2, a contention supported by the positive correlation between T_{EMO} and $X^b_{H_2O_2}$ ($r=0.87$, $n=22$, $P>0.99$).

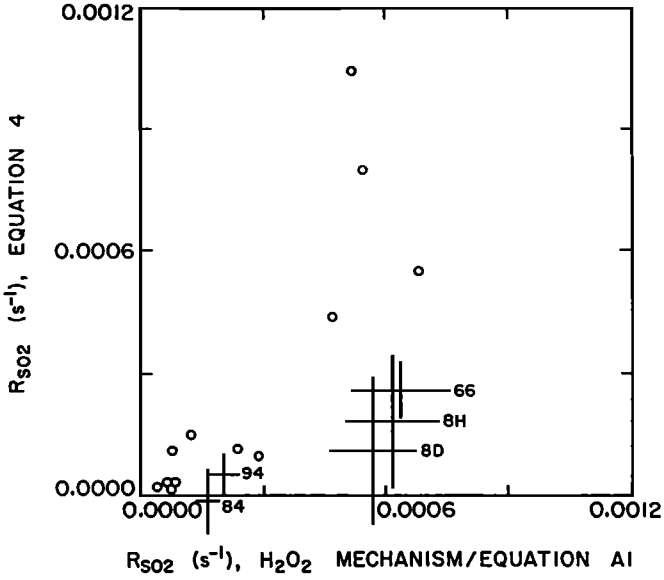

Figure 8. Comparison of R_{SO_2} values calculated from equation (A1) (abscissa) and values of R_{SO_2} derived using equation (4) (ordinate). Data values from experiments 84, 94, 8D, 8H, and 66 are labeled. Errors associated with these data values are also plotted. All other data pairs plot within one standard deviation of the 1:1 line.

Values of R_{SO_2} derived using (4) and R_{SO_2} values predicted using (A1), assuming the H_2O_2/S(IV) mechanism, are compared in Figure 8. A general agreement is found between observed and predicted values ($r=0.64$), however, five of the 17 calculated values are significantly larger than the observations. The numerical model results to be discussed below demonstrate that the H_2O_2/S(IV) reaction rate, expressed in ppbv s^{-1}, decreases near the end of the model simulations. Hence overprediction by (A1) results due to the assumption of steady state with respect to $X^b_{H_2O_2}$ and L^b_{EMO}, whereas the measurements are weighted both by the lower reaction rates expected near EMO due to the partial depletion of H_2O_2 and by the low values of LWC and the inefficient partitioning of H_2O_2 into the aqueous phase near cloud base. The large relative depletions of H_2O_2 (i.e., $D_{H_2O_2}/X^b_{H_2O_2} > 0.25$) which were observed during experiments 84, 94, and 66 can therefore be explained in terms of the argument just given. The remaining two cases of disagreement cannot be resolved in terms of the pseudo-first-order model; better agreement with observations is obtained for these cases with the analytic and numerical models (Table 8).

7.2. Numerical Model

Measured values of Y_{SO_4} and the results obtained from the numerical model (i.e., predicted total Y_{SO_4}) are compared in Figure 9. Experimental uncertainties, plotted as one standard deviation, for the three points which are a

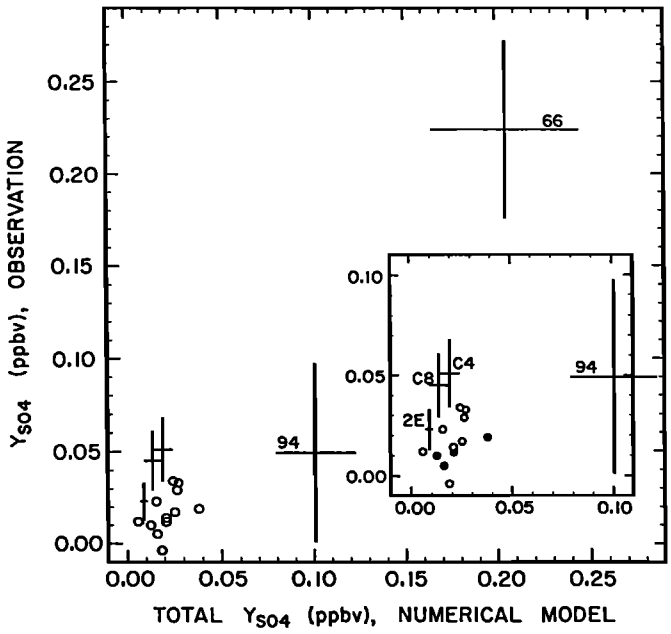

Figure 9. Comparison of values of total Y_{SO_4} predicted by the numerical model (abscissa) and observed values of Y_{SO_4} (ordinate). Data values that plot a significant distance above the 1:1 line (2E, C4, and C8) are labeled in the inset figure and plotted with error bars. Points 2G, 2J, 2L, and 2N are shown in the inset figure as solid circles. Points 94 and 66 are also labeled and plotted with error bars. The slope of the best fit line, forced through the origin, and calculated using only those data values indicated by either open or solid circles is 1.0 (±0.2).

significant distance above the 1:1 line (2E, C4, and C8) and for the two largest values of Y_{SO_4} (94 and 66) are also shown. The best fit line (forced through the origin) for all 17 points has a slope of 1.1 (±0.1). For the 12 points indicated with circles the slope of the best fit line forced through the origin is 1.0 (±0.2). None of the Y_{SO_4} pairs lie a significant distance below the 1:1 line.

Measured values of $D_{H_2O_2}$ and numerical model predictions of total $D_{H_2O_2}$ are illustrated in Figure 10. Experimental uncertainties are presented as in Figure 9. Two data pairs (84 and C4) lie a significant distance above the 1:1 line. The slope of the best fit line, forced through the origin (1.5±0.1, n = 15), taken together with the five outlying points shown in Figures 9 and 10, provides evidence that the numerical model may underpredict a few of the field measurements of $D_{H_2O_2}$ and Y_{SO_4}. However, this disparity may also reflect the previously discussed uncertainties associated with the temperature-extrapolated quantity $k_{8,1}K_{H,8}K_{H,2}K_{A1,2}$.

8. Discussion of Results

8.1. Principal Results

The results shown in Figures 8, 9, and 10 indicate agreement between observations and the predictions of the pseudo-first-order and the numerical models for the majority of cases. Also, H_2O_2 depletions obtained from the analytic model agree with the numerical model results. Based on this comparison and the agreement between the observations and the numerical model predictions of $D_{H_2O_2}$ shown in Figure 10, it appears that the analytic model can also be used with confidence to describe the in-cloud oxidation of S(IV) by H_2O_2.

Two simplifications included in the numerical model calculations need to be examined further. First, droplets are characterized by one time-dependent size and composition. Furthermore, thermodynamic control of ferric iron species concentrations is assumed. Second, the calculations represent processes within a closed parcel, i.e., mixing into the SO_2 plume is neglected. Uncertainties that result from these model assumptions are examined below.

8.2. Droplet Composition

Here we present model output corresponding to one of the experiments (2L) conducted on January 6, 1989 and discuss the equilibrium assumption concerning the dissolution of ferric hydroxide. For these experiments we note that (1) the field measurements of Y_{SO_4} are greater than $D_{H_2O_2}$ (Table 1), (2) the numerical model predictions of Y_{SO_4} are dominated by sulfate production via the O_2/S(IV) pathway (Table 8), and (3) that predictions of sulfate produced via the O_2/S(IV) pathway corresponding to experiments 2G, 2J, 2L, and 2N (indicated by solid circles in Figure 9) are larger than the observations of Y_{SO_4}.

Figures 11a-11d illustrate the time variations of the calculated values of LWC, droplet radius, concentrations of several dissolved species, and reaction rates expressed in ppbv s^{-1}. With the exception of the S(IV), S(VI), and the

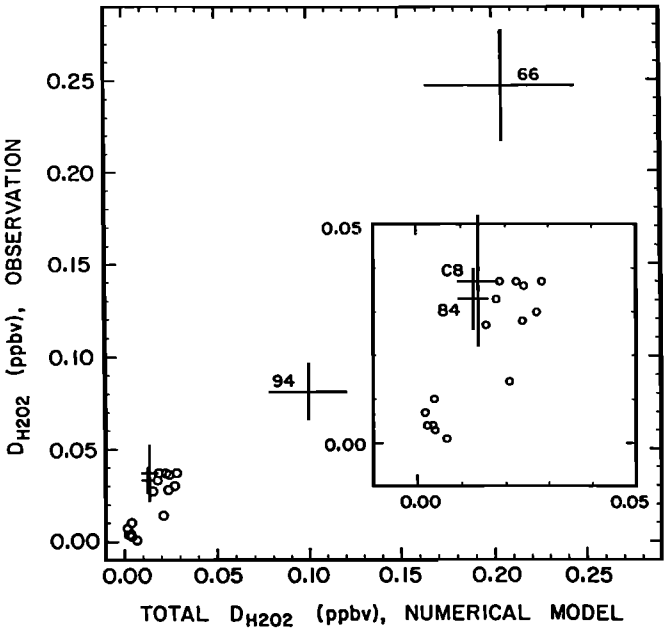

Figure 10. Comparison of values of total $D_{H_2O_2}$ predicted by the numerical model (abscissa) and observed values of $D_{H_2O_2}$ (ordinate). Data values that plot a significant distance above the 1:1 line (84 and C8) are labeled in the inset figure and plotted with error bars. Points 94 and 66 are also plotted with error bars. The slope of the best fit line, forced through the origin, and calculated using only those data values indicated by circles is 1.5 (±0.2).

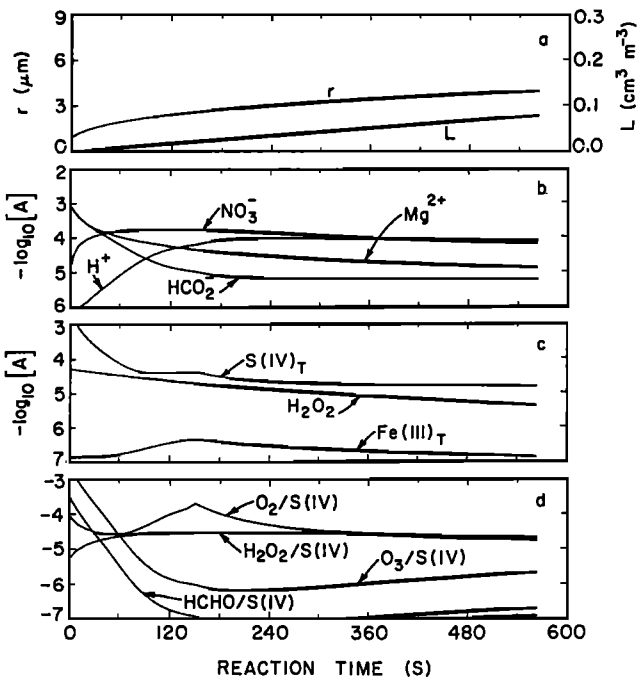

Figure 11. Predictions of the numerical model corresponding to experiment 2L. (a) Cloud droplet radius (r) and cloud water content (L); (b) $-\log_{10}[H^+]$, $-\log_{10}[HCO_2^-]$, $-\log_{10}[NO_3^-]$, and $-\log_{10}[Mg^{2+}]$; (c) $-\log_{10}[H_2O_2]$, $-\log_{10}[S(IV)]_T$, and $(-\log_{10}[Fe(III)]_T + 2)$; (d) reaction rates expressed as the decimal logarithm of the effective rates of reaction of O_2, O_3, H_2O_2, and HCHO with S(IV) in units of ppbv s^{-1}.

S(IV) coreactants the initial mixing ratios of all other model inputs (see Table 4) are conserved in the numerical model simulations. Hence the time-dependent concentrations of Mg^{2+}, NO_3^-, and HCO_2^- reflect the manner in which these constituents are incorporated into the cloud droplets. Magnesium ion is initialized as a soluble component of the cloud base aerosol, and it is therefore diluted in proportion to LWC. Both droplet radius and gas kinetic factors influence the dissolution of HNO_3, which occurs completely by t = 120 s, thereby forming NO_3^-, which is subsequently diluted in the same manner as Mg^{2+}. In contrast to Mg^{2+} and NO_3^- the value of $[HCO_2^-]$ is inversely correlated with $[H^+]$. This behavior is consistent with the assumed hydrogen ion and LWC-dependent partitioning of the formic acid species.

The quantity of cationic charge equivalents exceed those of anionic charge equivalents (i.e., $X_M > 2X_S + X_{Cl} + X_{AB}$; see Table 4) in the case of all experiments conducted on January 6, 1989. Therefore the initial value of $[H^+]$ in Figure 11b is small (4×10^{-7} M). Hydrogen ion increases by 2 orders of magnitude prior to t = 180 s due to S(VI) production, primarily via the O_3/S(IV) and O_2/S(IV) pathways, and by dissolution of HNO_3. The increase in $[H^+]$ is partially buffered by volatilization of S(IV) and formic acid species from the cloud droplets and by dissolution of $Fe(OH)_{3(s)}$; equilibrium constraints are assumed to control the extent of these buffering processes. The value of $[Fe(III)]_T$ is nearly constant prior to t = 60 s and then increases with $[H^+]$ prior to complete dissolution of $Fe(OH)_{3(s)}$ which is predicted to occur at t = 150 s. Dissolution of $Fe(OH)_{3(s)}$ results in the formation of sulfitoiron(III) complexes and buffers the values of $[S(IV)]_T$ at 40 μM. This behavior is consistent with the equilibrium calculations shown in Figures 7a and 7b. The rate of the O_2/S(IV) pathway, proportional to $[Fe(III)]_T$ and $[S(IV)]_T$ (see Table 7), is maximized at t = 150 s. Similar time variations of $[Fe(III)]_T$, $[S(IV)]_T$, and $[H^+]$ occur in model simulations corresponding to other experiments from January 6, 1989.

We believe that the dissolution kinetics of a solid phase containing Fe(III) may control the extent of sulfate production via the O_2/S(IV) pathway. Our hypothesis is supported by laboratory studies which indicate that dissolution of aerosols containing transition metals occurs on timescales much longer than air parcel transit times in orographic clouds [*Zhuang et al.*, 1992]. This is also supported by the fact that four of the five field measurements of Y_{SO_4} from January 6, 1989 are overpredicted by the numerical model.

Since the O_3/S(IV), the O_2/S(IV), and the HCHO/S(IV) pathways are sensitive to droplet *p*H, which in real clouds varies with aerosol size and composition and also with the size-dependent rate of droplet growth, substantial uncertainties in our model calculations may result from the uniform apportionment of ferric iron and other nonvolatile species. An assessment of even the direction of the biases introduced by these effects would require size-segregated measurements of the composition of the aerosol that participates in the condensation process.

8.3. Mixing

Neglecting mixing into the plume means (1) that SO_2 measurements from EMO can be used to model the reaction, (2) that no cloud water previously unaffected by plume SO_2 is brought into the parcel, and (3) that H_2O_2 is not replenished from outside the plume where less of it is consumed by reaction. The absence of mixing in the plume is inconsistent with LWC observations below adiabatic values (see section 4).

Because of cases 1 and 3 the model predictions of Y_{SO_4} and $D_{H_2O_2}$ are too low, whereas not considering case 2 makes the model prediction of Y_{SO_4} too high. A quantitative assessment of these effects is precluded by the lack of information about the details of mixing within the plume and by the model complexities that would be entailed. Upper limit estimates of the combined effects of cases 1 and 3 were obtained from the numerical model by prohibiting the depletion of H_2O_2 and by allowing for the time-dependent dilution of plume SO_2 using parameterizations of vertical and lateral plume dispersion coefficients obtained from *Karacostas* [1978]. Relative to the model results shown in Table 8 and excluding cases associated with the value of t_R greater than 8.7 min (discussed below), the averaged increases in the predicted values of total $D_{H_2O_2}$ and Y_{SO_4} were +26% and +21%, respectively. These biases are equal to or smaller than the experimental uncertainties reported in Table 1. Hence increases in the predicted values of $D_{H_2O_2}$ corresponding to the data points C8 and 84 shown in Figure 10 are not large enough to completely account for the disparity between model prediction and observation.

Factor of 2 or larger increases in the predicted values of

total $D_{H_2O_2}$ were found for nine model runs (89, 94, 2E, 2G, 2J, 2L, 2N, 66, and 8H). For these cases, all with values of t_R greater than 8.7 min (see Table 2) and factor of 2 or larger increases in wind speed between Brush Creek and the western summit of Elk Mountain, it is likely that the time over which the actual SO_2 plume interacted with regions of large LWC and low temperatures, factors favoring the production of sulfate via the H_2O_2/S(IV) pathway, was considerably shorter than predicted. For these nine cases the effect of mixing appears to be exaggerated. Overall, it appears that mixing introduces an inaccuracy in the comparison of the model predictions and the field measurements that is comparable to the experimental uncertainties.

9. Comparison With Other Results

In contrast with the dominance of H_2O_2/S(IV) and O_2/S(IV) pathways in our results, other investigators found that ozone is responsible for a significant fraction of sulfate production in orographic clouds. *Hegg and Hobbs* [1982] conducted airborne measurements of sulfate production near orographic clouds in western Washington State. They found agreement between derived values of sulfate production rate (corrected for mass transport limitations at *p*H values > 4.6) and reaction rates predicted by the kinetic rate expression for the O_3/S(IV) reaction [*Hoffmann*, 1986]. The clouds studied by *Hegg and Hobbs* [1982] were characterized by large *p*H values, typically exceeding 5. Their conclusion is consistent with the prediction of *Penkett et al.* [1979].

Using recently developed techniques for the continuous measurement of dissolved [*Ames*, 1983] and gas phase hydroperoxides [*Lazrus et al.*, 1986], *Clark et al.* [1990] conducted ground-based studies of SO_2 oxidation in springtime cap clouds at Great Dun Fell in northern England. These experiments reveal that sulfate is produced in nearly equal amounts via the H_2O_2/S(IV) and the O_3/S(IV) pathways. Using the cloud chemistry model of *Hill et al.* [1986], Clark et al. also examined the consequences of sulfate production, gaseous NH_3 and SO_2 absorption, the concomitant buffering of cloud water *p*H by NH_3 and SO_2 absorption, and the effects of these processes on the relative amount of sulfate produced by the O_3/S(IV) pathway. Their results, and earlier modeling [*Easter and Hobbs*, 1974] and observational studies [*Bamber et al.*, 1984], demonstrate the importance of gaseous ammonia in controlling the oxidation of SO_2 by O_3 in cloud systems where ammonia concentrations are sufficiently large to neutralize all of the strong acids incorporated into the cloud droplets.

Chandler et al. [1988a, b, and 1989] and *Gallagher et al.* [1990] reported measurements of H_2O_2 depletion and sulfate production in cap clouds at Great Dun Fell. By comparing field data to the predictions of a model [*Hill et al.*, 1986] they concluded that in-cloud H_2O_2/S(IV) reaction rates are enhanced by a factor of 3 to 10 relative to predictions based on laboratory kinetic and thermodynamic data. Laboratory studies of the reactive uptake of SO_2 gas by aqueous droplets containing H_2O_2 [*Jayne et al.*, 1990] indicate that the disparity between observed and predicted depletions of H_2O_2 at Great Dun Fell is probably not due to an enhanced rate of reaction between H_2O_2 and S(IV) on cloud droplet surfaces. *Clark et al.* [1990] hypothesize that the disparity is due to the postcollection reaction between H_2O_2 and S(IV), an explanation questioned by *Gallagher et al.* [1990] who assert that systematic errors in the Great Dun Fell field measurements are compensated by the competing effect of added H_2O_2 due to cloud entrainment.

Cloud temperatures during our wintertime experiments at Elk Mountain were 10° to 25°C colder than those of the orographic clouds at Great Dun Fell. Cloud water samples at Elk Mountain were obtained by riming, which is expected to exclude S(IV) and minimize errors due to reactions subsequent to sample collection. We have also accounted for postcollection reaction in our numerical model predictions of total Y_{SO_4} and total $D_{H_2O_2}$. For both reasons it is unlikely that the few values that plot above the 1:1 lines in Figures 9 and 10 are an artifact of reaction subsequent to cloud water collection. Direct and immediate measurements of $[S(IV)]_T$ and $[H_2O_2]$ in size-sorted droplets, both at Elk Mountain and at Great Dun Fell, would be required to fully assess the magnitude of this uncertainty. Such measurements would also help to substantiate or refute the validity of the reaction rate enhancements observed by *Chandler et al.* [1988a, b, and 1989] and by *Gallagher et al.* [1990]. Further differences between the Great Dun Fell and the Elk Mountain experiments are that at Elk Mountain there is little evidence for *p*H buffering by NH_3 or for the production of sulfate via the O_3/S(IV) reaction pathway.

10. Summary

Field measurements of the depletion of hydrogen peroxide and the production of sulfate in wintertime orographic clouds have been presented. Measurements of the sulfate yield and the hydrogen peroxide depletion indicate that H_2O_2 is the dominant SO_2 oxidant. The O_2/S(IV) pathway produced significant amounts of sulfate on one of the nine days experiments were conducted.

Our model calculations also indicate that ozone-mediated sulfate production is of minor importance in these clouds. This conclusion is supported by the field measurements of Y_{SO_4} and $D_{H_2O_2}$ and by the correlative relationships between R_{SO_2} and measurements of the physical and chemical properties of the cloud. However, we cannot completely rule out the significance of the O_3/S(IV) pathway since there are uncertainties with regard to the distribution of solute as a function of droplet size and because droplets smaller than 2 μm were not efficiently collected.

In contrast to the striking inconsistency between laboratory measurements and the apparent rate of the H_2O_2/S(IV) reaction in clouds at Great Dun Fell, most of the observations of $D_{H_2O_2}$ at Elk Mountain are consistent with model predictions. This result, taken together with both the explanation of the discrepancy between observed and calculated H_2O_2 depletions in Great Dun Fell clouds provided by *Clark et al.* [1990] and with the results of the laboratory studies conducted by *Jayne et al.* [1990], demonstrates that the laboratory measurements of the rate of S(IV) oxidation by H_2O_2 provide an adequate basis for inferring the rate of this reaction in supercooled clouds similar to those studied at Elk Mountain.

Appendix: Descriptions of the Pseudo-First-Order and Analytic Models

Pseudo-First-Order Model

The pseudo-first-order reaction rate was deduced using the expression

$$R_{SO_2} = E/\tau_i \quad \text{(A1)}$$

and measurements of $X^p_{SO_2}$, T_{EMO}, and background measurements of *p*H, $X^b_{SO_2}$, L^b_{EMO}, $X^b_{H_2O_2}$ and X_{O_3}. In (A1), τ_i is the chemical lifetime of the dissolved S(IV) species corresponding to a reaction pathway specified by the subscript "i", and E is the equilibrium fraction of S(IV) species dissolved in the cloud water. It is assumed that the only aqueous phase S(IV) species are SO_2^{2-}, HSO_3^-, and SO_2; τ_i is a function of temperature-dependent rate and equilibrium constants, background measurements of *p*H, oxidant mixing ratio, and a function of L^b_{EMO} in the case of highly soluble S(IV) coreactants. E is a function of the solubility of SO_2 (temperature dependent) and L^b_{EMO}. From (A1), R_{SO_2} is expected to increase with increases in oxidant mixing ratio, and LWC in the case of the O_3/S(IV) reaction pathway, decrease with increasing T_{EMO}, decrease with increasing $[H^+]$ in the case of the O_3/S(IV) reaction, and be nearly invariant with $[H^+]$ and LWC in the case of the H_2O_2/S(IV) reaction.

Analytic Model

As summarized in Table 3 and in contrast to the pseudo-first-order model, the analytic model accounts for the time dependence of LWC and reagent depletion. Analytic model predictions of the extent of reaction (Z, mol m^{-3}) resulting from the oxidation of dissolved S(IV) by H_2O_2 is obtained by solution of the rate law (A2).

$$\frac{dZ}{dt} = L(t)k_8[HSO_3^-][H_2O_2] \quad \text{(A2)}$$

In (A2) the pseudo-second-order rate constant (k_8, M s^{-1}) is a function of T_{EMO}, background measurements of *p*H, and $k_{8,1}$ (see Table 7). It is assumed that L(t) is a linear function of time (see (7)), that temperature = T_{EMO} and pressure = P_{EMO} are constant, and that the dissolved concentrations of S(IV) and H_2O_2 are the saturated values predicted by Henry's law. These assumptions are also required to run the numerical model.

Four additional assumptions are required to integrate (A2): (1) HSO_3^- is assumed to be consumed only by reaction with H_2O_2; (2) dissolved SO_2, HSO_3^-, and SO_3^{2-} are assumed to be the only S(IV) species in solution; (3) the activity of HSO_3^- is assumed equal to its concentration; and (4) cloud water *p*H is assumed constant. Given the fact that the quantity $k_8[HSO_3^-]$ is nearly independent of *p*H, the final assumption is valid. The accuracy of predictions provided by the analytical model, compared to the numerical model, is therefore limited in situations where additional loss processes exist for cloud water dissolved S(IV) and H_2O_2 and where solution ionic strength is greater than 10^{-4}M.

The rate of reaction between S(IV) and H_2O_2 can be expressed as a function of the extent of reaction (Z, mol m^{-3}), the initial partial pressures of H_2O_2 ($P_{0,8}$, Pa) and SO_2 ($P_{0,2}$, Pa), and the enhanced Henry's law coefficient ($K^*_{H,2}$, M Pa^{-1}).

$$\frac{dZ}{dt} = \frac{k_8C_1L(t)K_{H,2}K_{A1,2}K_{H,8}(P_{0,2} - ZRT)(P_{0,8} - ZRT)}{[H^+](1.+K^*_{H,2}C_1L(t)RT)(1.+ K_{H,8}C_1L(t)RT)} \quad \text{(A3)}$$

Equation (A3) is a separable differential equation. Separating the variables Z and t, using partial fractions and the initial conditions Z(0) = 0.0, we have

$$Z(t) = \frac{P_{0,8}P_{0,2}(G(t)^{\omega} - 1.)}{RT(P_{0,8}G(t)^{\omega} - P_{0,2})} \quad \text{(A4)}$$

where

$$G(t) = \frac{(1.+K^*_{H,2}C_1L_{CB}RT)(1.+K_{H,8}C_1L(t)RT)^{\xi}}{(1.+K^*_{H,2}C_1L(t)RT)(1.+K_{H,8}C_1L_{CB}RT)^{\xi}} \quad \text{(A5)}$$

$$\omega = \frac{t_Rk_8K_{H,2}K_{A1,2}K_{H,8}(P_{o,8} - P_{o,2})}{RT[H^+]C_1(L^b_{EMO} - L_{CB})(\xi - 1.)} \quad \text{(A6)}$$

$$\xi = K^*_{H,2} / K_{H,8} \quad \text{(A7)}$$

Values of $D_{H_2O_2}$ were calculated as the difference between values of $Z(t = t_R)$, corresponding to $X^p_{SO_2}$ and $X^b_{SO_2}$, multiplied by the molar volume of air evaluated at T_{EMO} and P_{EMO}.

Acknowledgments. Assistance provided by the staff of the Department of Atmospheric Science is greatly appreciated. This work was supported by National Science Foundation grants ATM-8715294 and ATM-9012805.

References

Ames, D. L., A method of determining hydrogen peroxide in cloud and rainwater, *CEGB Note NO.TPRD/L/2552 N83*, Cent. Elect. Generating Board, Leatherhead, Surrey, England, 1983.

Bamber, D. J., P. A. Clark, G. M. Glover, P. G. W. Healey, A. S. Kallend, A. R. W. Marsh, A. F. Tuck, and G. Vaughan, Air sampling flights round the British Isles at low altitudes: SO_2 oxidation and removal rates, *Atmos. Environ.*, *18*, 1777-1790, 1984.

Bell, R. P., The reversible hydration of carbonyl compounds, in *Advances in Physical Organic Chemistry*, *4*, edited by V. Gold, pp. 1-28, 1966.

Boyce, S., and M. R. Hoffmann, Kinetics and mechanism of the formation of hydroxymethanesulfonic acid at low *p*H, *J. Phys. Chem.*, *88*, 4740-4746, 1984.

Brock, F. V., G. H. Saum, and S. R. Semmer, Portable automated mesonet II, *J. Atmos. Oceanic Technol.*, *3*, 573-582, 1986.

Calvert, J. G., A. Lazrus, G. L. Kok, B. G. Heikes, J. G. Walega, J. Lind, and C. A. Cantrell, Chemical mechanisms of acid generation in the troposphere, *Nature*, *317*, 27-35, 1985.

Chameides, W. L., The photochemistry of a remote marine stratiform cloud, *J. Geophys. Res.*, *89*, 4739-4756, 1984.

Chandler, A. S., T. W. Choularton, G.J. Dollard, M.J. Gay, T.A. Hill, A. Jones, B. M. R. Jones, A.P. Mores, S.A. Penkett, and B.J. Tyler, A field study of cloud chemistry and cloudmicrophysics at Great Dun Fell, *Atmos. Environ.*, *22*, 683-694, 1988a.

Chandler, A. S., T. W. Choularton, G. J. Dollard, A. E. J. Eggleton, M. J. Gay, T. A. Hill, B. M. R. Jones, B. J. Tyler, B. J. Bandy, and S. A. Penkett, Measurements of H_2O_2 and SO_2 in clouds and estimates of their reaction rate, *Nature*, *336*, 562-565, 1988b.

Chandler, A. S., T. W. Choularton, G. J. Dollard, M. J. Gay, M. W. Gallagher, T. A. Hill, B. M. R. Jones, S. A. Penkett, B. J. Tyler, and B. Bandy, A field study of the oxidation of SO_2 incap cloud at Great Dun Fell, *Q. J. R. Meteorol. Soc.*, *115*, 397-420, 1989.

Clark, P. A., G. P. Gervat, T. A. Hill, A. R. W. Marsh, A. S. Chandler, T. W. Choularton, and M. J. Gay, A field study of the oxidation of SO_2 in cloud, *J. Geophys. Res.*, *95*, 13,985-13,995, 1990.

Conklin, M. H., and M. R. Hoffmann, Metal ion - S(IV) chemistry, III, Thermodynamics and kinetics of transient iron(III)-sulfur(IV) complexes, *Environ. Sci. Technol.*, *22*, 899-907, 1988.

Drever, J. I., *The Geochemistry of Natural Waters*, 2nd ed., 437 pp., Prentice-Hall, Englewood Cliffs, N. J., 1988.

Easter, R. C., and P. V. Hobbs, The formation of sulfates and the enhancement of cloud condensation nuclei in clouds, *J. Atmos. Sci.*, *31*, 1586-1594, 1974.

Fuchs, N. A., and A. G. Sutugin, High dispersed aerosols, in *Topics in Current Aerosol Research*, II, edited by G. M. Hidy and J. R. Brock, pp. 1-60, Pergamon, New York, 1971.

Gallagher, M. W., et al., Case studies of the oxidation of sulfur dioxide in a hill cap cloud using ground- and aircraft-based measurements, *J. Geophys. Res.*, *95*, 18,517-18,537, 1990.

Gervat, G. P, P. A. Clark, A. R. W. Marsh, I. Teasdale, A. S. Chandler, T. W. Choularton, M. J. Gay, M. K. Hill, and T. A. Hill, Field evidence for the oxidation of SO_2 by H_2O_2 in cap clouds, *Nature*, *333*, 241-243, 1988.

Hegg, D. A. and P. V. Hobbs, Measurement of sulfate production in natural clouds, *Atmos. Environ.*, *16*, 2663-2668, 1982.

Hegg, D. A., and P. V. Hobbs, Comparisons of measured sulfate production due to ozone oxidation in clouds with a kinetic rate equation, *Geophys. Res. Lett.*, *14*, 719-721, 1987.

Hegg, D. A., and T. V. Larson, The effect of microphysical parameterization on model predictions of sulfate production in clouds, *Tellus*, *42(B)*, 272-284, 1990.

Hill, T. A., T. W. Choularton, and S. A. Penkett, A model of sulfate production in a cap cloud and subsequent turbulent deposition onto the hill surface, *Atmos. Environ.*, *20*, 1763-1771, 1986.

Hoffmann, M. R., On the kinetics and mechanisms of oxidation of aquated sulfur dioxide by ozone, *Atmos. Environ.*, *20*, 1145-1154, 1986.

Hoffmann, M. R., and J. G. Calvert, Chemical transformation modules for Eulerian acid deposition models, Vol. II, The aqueous-phase chemistry, *Rep. EPA/600/3-85/017*, Environ. Prot. Agency, Research Triangle Park, N. C., 1985.

Ibusuki, T., and K. Takeuchi, sulfur dioxide oxidation by oxygen catalyzed by mixtures of manganese(II) and iron(III) in aqueous solutions at environmental reaction conditions, *Atmos. Environ.*, *21*, 1555-1560, 1987.

Iribarne, J. V., T. Pyshnov, and B. Naik, The effect of freezing on the composition of cloud droplets - II. Retention of S(IV), *Atmos. Environ.*, *24(A)*, 389-398, 1990.

Jacob, D. J., E. W. Gottlieb, and M. J. Prather, Chemistry of a polluted cloudy boundary layer, *J. Geophys. Res.*, *94*, 12,975-13,002, 1989.

Jayne, J. T., J. A. Gardner, P. Davidovits, D. R. Worsnop, M. S. Zahniser, and C. E. Kolb, The effect of H_2O_2 content on the uptake of SO_2(g) by aqueous droplets, *J. Geophys. Res.*, *95*, 20,559-20,563, 1990.

Karacostas, T. S., Transport and turbulent diffusion over mountainous terrain, Ph.D. Dissertation, Univ. of Wyoming, Laramie, 1978.

Keene, W. C., and J. N. Galloway, Considerations regarding sources for formic and acetic acid in the troposphere, *J. Geophys. Res.*, *91*, 14,466-14,474, 1986.

Kim, Y. J., H. Sievering, and J. F. Boatman, Airborne measurement of atmospheric aerosol particles in the lower troposphere over the central United States, *J. Geophys. Res.*, *93*, 12,631-12,644, 1988.

King, W. D., D. A. Parkin, and R. J. Handsworth, A hot-wire liquid water device having fully calculable response characteristics, *J. Appl. Meteorol.*, *17*, 1809-1813, 1978.

Kirchner, W., F. Welter, A. Bongartz, J. Kames, S. Schweighoefer, and U. Schurath, Trace gas exchange at the air/water interface: Measurement of mass accommodation coefficients, *J. Atmos. Chem.*, *10*, 427-449, 1990.

Kok, G. L., K. Thompson, A. L. Lazrus, and S. E. McLaren, Derivatization technique for the determination of peroxides in precipitation, *Anal. Chem.*, *58*, 1192-1194, 1986.

Lamb, D., and R. Blumenstein, Measurement of the entrapment of sulfur dioxide by rime ice, *Atmos. Environ.*, *21*, 1765-1772, 1987.

Langmuir, I., and K. B. Blodgett, Mathematical investigation of water-droplet trajectories, *U.S. Air Force Tech. Rep. 5418*, U.S. Army Air Forces, 1946.

Lawson, D. R., and J. W. Winchester, Sulfur and crustal reference elements in nonurban aerosols from Squaw Mountain, Colorado, *Environ. Sci. Technol.*, *12*, 716-721, 1978.

Lazrus, A. L., G. L. Kok, J. A. Lind, S. N. Gitlin, B. G. Heikes, and R. E. Shetter, Automated fluorometric method for hydrogen peroxide in air, *Anal. Chem.*, *58*, 594-597, 1986.

Lee, Y. N., J. Shen, P. J. Klotz, S. E. Schwartz, and L. Newman, Kinetics of hydrogen peroxide-sulfur(IV) reaction in rainwater collected at a northeastern U.S. site, *J. Geophys. Res.*, *91*, 13,264-13,274, 1986.

Levin, Z., C. Price, and E. Ganor, The contribution of sulfate and desert aerosols to the acidification of clouds and rain in Israel, *Atmos. Environ.*, *24(A)*, 1143-1151, 1990.

Lind, J. A., and G. L. Kok, Henry's law determination for aqueous solutions of hydrogen peroxide, methylhydrogen peroxide, and peroxyacetic acid, *J. Geophys. Res.*, *91*, 7889-7895, 1986.

Lind, J. A., A. L. Lazrus, and G. L. Kok, Aqueous phase oxidation of sulfur(IV) by hydrogen peroxide, methylhydroperoxide, and peroxyacetic acid, *J. Geophys. Res.*, *92*, 4171-4178, 1987.

Maahs, H. G., Sulfur dioxide/water equilibria between 0° and 50° C, An examination of data at low concentrations, in *Heterogeneous Atmospheric Chemistry*, *Geophys. Monog. Ser.*, vol. 26, edited by D. R. Schryer, pp. 187-195, AGU, Washington, D. C., 1982.

Munger, J. W., J. Collett, B. Daube, and M. R. Hoffmann, Chemical composition of coastal stratus clouds: Dependence on droplet size and distance from the coast, *Atmos. Environ.*, *23*, 2305-2320, 1989.

Pandis, S. N., and J. H. Seinfeld, Should bulk cloudwater or fogwater samples obey Henry's law?, *J. Geophys. Res.*, *96*, 10,791-10,798, 1991.

Penkett, S. A., B. M. R. Jones, K. A. Brice, and A. E. J. Eggleton, The importance of atmospheric ozone and

hydrogen peroxide in oxidizing sulfur dioxide in cloud and rainwater, *Atmos. Environ.*, *13*, 123-137, 1979.

Perdue, E. M., and K. C. Beck, Chemical consequences of mixing atmospheric droplets of varied pH, *J. Geophys. Res.*, *93*, 691-698, 1988.

Politovich, M. K., and G. Vali., Observations of liquid water in orographic clouds over Elk Mountain, *J. Atmos. Sci.*, *40*, 1300-1312, 1983.

Radojevic, M., B. J. Tyler, A. J. Wicks, M. J. Gay, and T. W. Choularton, Field studies of the SO_2/aqueous S(IV) equilibrium in clouds, *Atmos. Environ.*, *(24A)*, 323-328, 1990.

Rancourt, R. L., and J. B. Howe, On the distribution of acidity within clouds as a function of droplet size, *Mt. Wash. Obs. News Bull.*, *28*, 48-52, 1987.

Rogers, D. C., D. Baumgardner, and G. Vali, Determination of supercooled liquid water content by measuring rime rate, *J. Clim. Appl. Meteorol.*, *22*, 153-162, 1983.

Snider, J. R., Measurement of sulfur dioxide reaction rates in wintertime orographic clouds, Ph.D. dissertation, 341 pp., Univ. of Wyoming, 1989.

Snider, J., D. C. Montague, and G. Vali, Hydrogen peroxide retention in rime ice, *J. Geophys. Res.*, *97*, 7569-7578, 1992.

Stumm, W., and J. J. Morgan, *Aquatic Chemistry*, John Wiley, New York, 1970.

Van Doren, J. M., L. R. Watson, P. Davidovits, D. R. Worsnop, M. S. Zahniser, and C. E. Kolb, The temperature dependence of the uptake of HNO_3, HCl, and N_2O_5 by water droplets, *J. Phys. Chem.*, *94*, 3265-3269, 1990.

Warneck, P. N., *Chemistry of the Natural Atmosphere*, 753 pp., Academic, San Diego, Calif., 1988.

Weast, R. C. (Ed.), Handbook of Chemistry and Physics, 63rd ed., Chemical Rubber Company, Cleveland, Ohio, 1982.

Zhuang, G., Z. Yi, R. A. Duce, and P. R. Brown, Chemistry of iron in marine aerosols, *Global Biochem. Cycles*, *6*, 161-173, 1992.

J.R. Snider and G. Vali, Department of Atmospheric Science, University of Wyoming, Laramie, WY 82071.

(Received March 10, 1993; revised April 1, 1994; accepted June 8, 1994.)